

CONFERENCES AND SYMPOSIA

PACS numbers: 01.10.Fv, **03.75. – b**, **07.57. – c**, 32.30.Jc, **37.10. – x**, 37.10.De, 37.10.Gh, **42.62. – b**, **42.65. – k**, **42.70. – a**, **42.82. – m**, **67.85. – d**,**78.67. – n**, **85.40. – e**, 84.40.Ik

Celebrating 50 years of the laser (Scientific session of the General Meeting of the Physical Sciences Division of the Russian Academy of Sciences, 13 December 2010)

DOI: 10.3367/UFNe.0181.201108e.0867

A scientific session of the general meeting of the Physical Sciences Division of the Russian Academy of Sciences (RAS) dedicated to the 50th anniversary of the creation of lasers was held in the Conference Hall of the Lebedev Physical Institute, RAS, on 13 December 2010.

The agenda of the session announced on the website www.gpad.ac.ru of the RAS Physical Sciences Division listed the following reports:

(1) **Matveev V A, Bagaev S N** Opening speech;

(2) **Bratman V L, Litvak A G, Suvorov E V** (Institute of Applied Physics, RAS, Nizhny Novgorod) "Mastering the terahertz domain: sources and applications";

(3) **Balykin V I** (Institute of Spectroscopy, RAS, Troitsk, Moscow region) "Ultracold atoms and atom optics";

(4) **Ledentsov N N** (Ioffe Physical Technical Institute, RAS, St. Petersburg) "New-generation surface-emitting lasers as the key element of the computer communication era";

(5) **Krasil'nik Z F** (Institute for the Physics of Microstructures, RAS, Nizhny Novgorod) "Lasers for silicon optoelectronics";

(6) **Shalagin A M** (Institute of Automation and Electrometry, Siberian Branch, RAS, Novosibirsk) "High-power diode-pumped alkali metal vapor lasers";

(7) **Kul'chin Yu N** (Institute for Automation and Control Processes, Far Eastern Branch, RAS, Vladivostok) "Photonics of self-organizing biomineral nanostructures";

(8) **Kolachevsky N N** (Lebedev Physical Institute, RAS, Moscow) "Laser cooling of rare-earth atoms and precision measurements."

The papers written on the basis of reports 2–4, 7, and 8 are published below.*

* Because the paper based on report 6 was received by the Editors late, it will be published in the October issue of *Physics–Uspekhi* together with the material related to the Scientific Session of the Physical Sciences Division, RAS, of 22 December 2010.

Uspekhi Fizicheskikh Nauk **181** (8) 867 – 903 (2011)
DOI: 10.3367/UFNr.0181.201108e.0867
Translated by E N Ragozin and M Sapozhnikov;
edited by A M Semikhatov and A Radzig

PACS numbers: **07.57. – c**, **42.62. – b**, 84.40.Ik
DOI: 10.3367/UFNe.0181.201108f.0867

Mastering the terahertz domain: sources and applications

V L Bratman, A G Litvak, E V Suvorov

1. Introduction

The terahertz range, which is intermediate in position between the microwave and optical portions of the electromagnetic spectrum, for a long time remained the least mastered, and seemed to be too short in wavelength for the methods of classical vacuum electronics and too low in frequency for the methods of quantum electronics to be applied. At the same time, this range has several specific features that make it highly attractive for a wealth of basic and applied studies in the areas of physics, chemistry, biology, and medicine [1–3]. The point is that this range comprises many strong lines of rotational molecular transitions, as well as lines of the vibrational and vibrational–rotational transitions of large molecules, including organic ones, which opens up possibilities for their investigation and for selective action on them. Terahertz waves show promise for the diagnostics and spectroscopy of various media, including the development of high-resolution methods of electron paramagnetic resonance (EPR) and nuclear magnetic resonance (NMR). High-power terahertz radiation can be used to produce dense plasmas and control their parameters (controlled fusion, point-like plasma X-ray radiation sources).

Owing to its low photon energy, terahertz radiation is relatively safe for living organisms and can be used for the detection of pathologies and foreign masses by terahertz tomography techniques [4, 5]. Terahertz radiation has a relatively high penetration power and can therefore be used for the detection and identification of objects concealed by clothes, packaging, and even concrete walls. The methods of terahertz time-domain spectroscopy based on the application of broadband coherent pulses provide a fast covering of a broad frequency range, thereby making it possible to reveal the characteristic spectral features ('fingerprints') of different

V L Bratman, A G Litvak, E V Suvorov Institute of Applied Physics, Russian Academy of Sciences, Nizhny Novgorod, Russian Federation
E-mail: bratman@appl.sci-nnov.ru

Uspekhi Fizicheskikh Nauk **181** (8) 867 – 874 (2011)
DOI: 10.3367/UFNr.0181.201108f.0867
Translated by E N Ragozin; edited by A M Semikhatov

molecules. This is important for the detection and identification of plastic explosives, hazardous chemicals, and narcotic drugs, for conducting express analysis of the composition of breathe air for the purposes of diagnosing various diseases, for monitoring the quality of foods, for inspecting agricultural products, and so on [6, 7]. Short coherent terahertz radiation pulses permit studying fast processes. This list does not exhaust the field of possible applications involving the use of terahertz radiation and is constantly expanding [1, 2].

The term 'terahertz range' is used in reference to the frequency range from 0.1 to 10 THz (wavelengths from 3 to 0.03 mm), which covers the short-wavelength part of the millimeter range well mastered by vacuum electronics, as well as the entire range of submillimeter waves and a part of the far-infrared region. Mastering the terahertz range includes creating sources and means of registration, as well as developing diverse applications. Our report is a brief review of the achievements in the generation of terahertz radiation by the methods of classical vacuum electronics and optoelectronics,[1] in addition to several applications of terahertz radiation.

Among the most widespread vacuum sources of coherent terahertz radiation are backward-wave oscillators (BWOs), which rely on stimulated Cherenkov radiation by straight electron beams, and high-power free-electron lasers (FELs) and gyrotrons, which rely on the stimulated bremsstrahlung of curved beams. All these devices have been adequately developed in Russia. Low-voltage BWOs with the oscillation frequency up to 1.4 THz [9], which are manufactured by the ISTOK company, have found wide use in numerous applications in Russia and abroad. The FEL with the particle energy up to 12 MeV created at the Budker Institute of Nuclear Physics (INP), Siberian Branch, RAS, presently provides the record high level of average coherent radiation power in the 1.2–1.8 THz range at the fundamental harmonic of the particle oscillation frequency and also operates at the harmonics of this frequency [10]. As shown in Section 2, the gyrotrons developed at the Institute of Applied Physics (IAP), RAS, demonstrate the feasibility of generating high-power radiation up to the frequencies of at least 1.5 THz for substantially lower particle energies (several tens of keV) than in FELs [11]. Although a start on the use of optoelectronic techniques in the terahertz range was made in Russia later than abroad, it was not long before the area covering the search for new materials and generation techniques and schemes, as well as the demonstration of possible applications, was brought up to date.

2. Classic vacuum sources

Low-voltage compact BWOs [9] provide the output radiation power of the order of 30–1 mW for waves with the frequencies 0.1–1.4 THz. There is also a higher-power but more narrowly used version of a BWO with an electron beam tilted with respect to a slow-wave structure — a 'klinotron,' which operates at frequencies up to a value of the order of 0.5 THz [12]. To improve its efficiency, however, this oscillator uses a mode with substantial reflections of the working wave from the structure ends, which makes this device sensitive to frequency tuning. Among the devices with straight electron beams that show promise for the terahertz range, we also note extended interaction klystrons [13], which give a very high performance throughout the millimeter range, and orotrons (or diffraction radiation generators). The pulsed orotrons recently developed at the IAP jointly with the National Research Institute for Physicotechnical and Radio Engineering Measurements and the Institute of Spectroscopy, RAS, have reached the output frequency 0.4 THz for a relatively smooth electromechanical frequency tuning over a very broad range (up to 1–1.5 octaves) and the output power of several hundred mW [14].

[1] Research in semiconductor terahertz oscillators is reviewed, e.g., in Ref. [8].

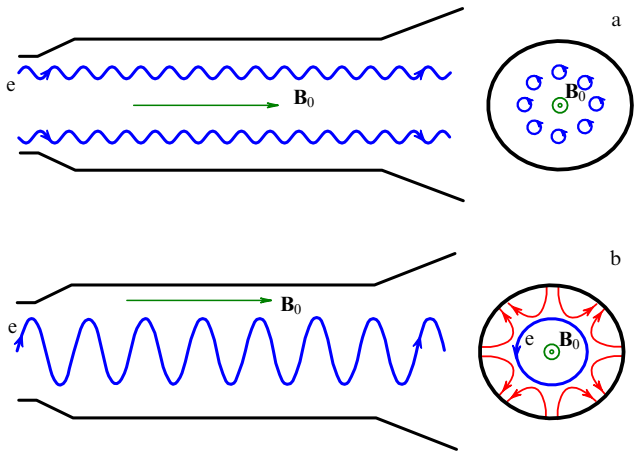

Figure 1. Workspace of (a) a conventional gyrotron with a polyaxial electron beam and (b) a large-orbit gyrotron with a monoaxial electron beam.

Unlike devices with straight electron beams, FELs and gyrotrons use stimulated bremsstrahlung of the electrons that follow periodic trajectories. In these devices, the particles interact with fast eigenwaves. This permits using large-volume open resonators or waveguides as electrodynamic structures and exciting them by high-intensity electron beams traveling far from the structure walls. This allows obtaining a very high output power.

In a gyrotron (Fig. 1), electrons move along helical trajectories in a uniform magnetic field $\mathbf{B}_0$ of a solenoid and interact with the high-frequency field of a cylindrical resonator under the cyclotron resonance condition

$$\omega \approx s\omega_c \,, \tag{1}$$

where ω is the field frequency, $s = 1, 2, \ldots$ is the number of a resonance cyclotron harmonic, and $\omega_c = eB_0/m\gamma$ is the cyclotron frequency, where e, m, and γ are the electron charge, mass, and relativistic factor. Of fundamental importance for all particle energies is the nonisochronicity of cyclotron rotation caused by the relativistic energy dependence of the cyclotron frequency, which results in azimuthal bunching of the particles in Larmor circles under the effect of the amplified (seed) wave. For this bunching to develop, the rotational electron velocity should be high enough and the interaction space should be sufficiently long.

To minimize the Doppler broadening of the cyclotron resonance line, modes with the lowest longitudinal wavenumber are used in gyrotrons. Accordingly, for a resonator length much longer than the wavelength, the operating mode field is composed of the waves that propagate nearly transversely to the magnetic field. That is why it is possible to neglect the Doppler correction to the frequency under resonance condition (1) (in detailed calculations, especially for beams with a substantial spread of particle velocities, this frequency shift,

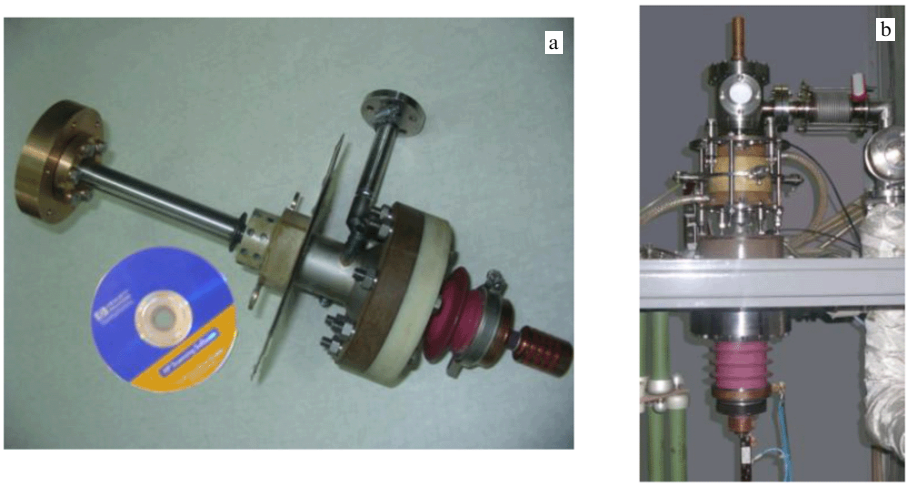

Figure 2. Photographs of pulsed terahertz gyrotrons made at the IAP, which operate (a) at the main cyclotron resonance and (b) at higher-order harmonics.

which is in particular responsible for the inhomogeneous broadening of the cyclotron resonance line, should be taken into account).

Condition (1) implies a formula for the resonance magnitude of the magnetic field,

$$B_0(T) = 35.7\,\frac{\gamma}{s}\,f\ [\mathrm{THz}]\,, \qquad (2)$$

whence it follows that terahertz gyrotrons using the fundamental $(s = 1)$ cyclotron resonance require very strong magnetic fields: obtaining a 1 THz frequency requires a field above 36 T. At the present time, such fields can be produced primarily by pulsed solenoids. But when ensuring efficient discrimination against parasitic modes, the high-frequency oscillation can also be obtained at higher-order harmonics, when the working magnetic field is s times lower and can be produced in modern cryomagnetic systems. As a result, for much lower particle energies and far smaller device dimensions, the gyrotrons, according to estimates, are capable of operating at the same or even higher power levels as FELs, at the frequencies up to 1–1.5 THz in pulsed and cw modes.

In the first experiments with terahertz gyrotrons carried out at the IAP in the 1970s–1980s, demonstration experiments were performed on cw oscillation at the second harmonic at the frequency 0.33 THz with a power at the kilowatt level [15] and the 50 μs single-pulse generation at the fundamental cyclotron resonance at frequencies up to 0.65 THz with the peak power $10^4 - 10^5$ W [16]. Following this work, a start was made on the development of high-frequency gyrotrons by several groups in the USA, Australia, and Japan. At present, several organizations, including the IAP, are developing cw gyrotrons with frequencies lying in the range 0.14–0.52 THz, which are intended for EPR spectroscopy and dynamic nuclear polarization (DNP) in the high-field NMR spectroscopy [17–20], as well as for other applications. In the experiment carried out jointly by the IAP and Fukui University (Japan), a high-efficiency cw gyrotron was made at the main cyclotron resonance with the frequency 0.3 THz and the output power 2.7 kW, which uses a so-called liquid-helium-free cryogenic magnet with a field of 12 T [21]. Recently, gyrotrons operating at the main [22], second [23], and third [24] cyclotron harmonics overcame the 1 THz frequency mark. Despite the problems related to the production of high magnetic fields, such oscillators are relatively simple, affordable, and easily reproducible sources of high-power radiation.

It worth noting that in greatest demand currently are high-power subterahertz gyrotrons intended for electron cyclotron plasma heating and control of plasma parameters in controlled thermonuclear fusion facilities; when operated in a quasi-cw regime, they provide the output power 1 MW at a fairly high frequency (170 GHz) [25]. For the level of parasitic mode discrimination reached in the gyrotrons, the peak output power decreases relatively slowly with increasing frequency, but the average output power decreases at least as $\lambda^{5/2}$ due to the thermal problems arising from a decrease in the resonator surface and an increase in the fraction of ohmic losses in its walls.

To increase the output frequency of gyrotrons, a previously employed compact highly robust solenoid was recently improved at the IAP [16]. This allowed strengthening its magnetic field by a factor of two (to 50 T) and, for a particle energy up to 24 keV, generating several modes with frequencies in the $1-1.3$ THz range and the peak power 5–0.5 kW at the fundamental cyclotron resonance in a single-pulse mode (Fig. 2a) [22, 11]. Also under development at the IAP is a technology that will allow making relatively simple pulsed solenoids with the magnetic field up to 30 T and the repetition rate up to 0.1 Hz. This will result in the realization of conventional gyrotrons at the main cyclotron resonance and the second harmonic with the oscillation frequency up to 0.8–1.6 THz for the peak power of several hundred kilowatts and the average output power about 1 W.

In the operation at the main cyclotron resonance and the second harmonic, in terahertz gyrotrons, as in the millimeter range, tubular polyaxial electron beams are most frequently used (Fig. 1a). In the operation at higher-order harmonics, a stronger electron–wave coupling and a higher level of parasitic mode discrimination are realized for a nearly monoaxial (Fig. 1b) configuration of the electron beam, which is coaxial with an axially symmetric resonator. Under this geometry, which is used in the so-called large-orbit gyrotrons (LOGs), the field of the azimuthally rotating mode with an azimuthal index s perfectly coincides near the axis with the field of the $2s$th rotating multipole, which rotates synchronously with electrons that rotate in Larmor circles in

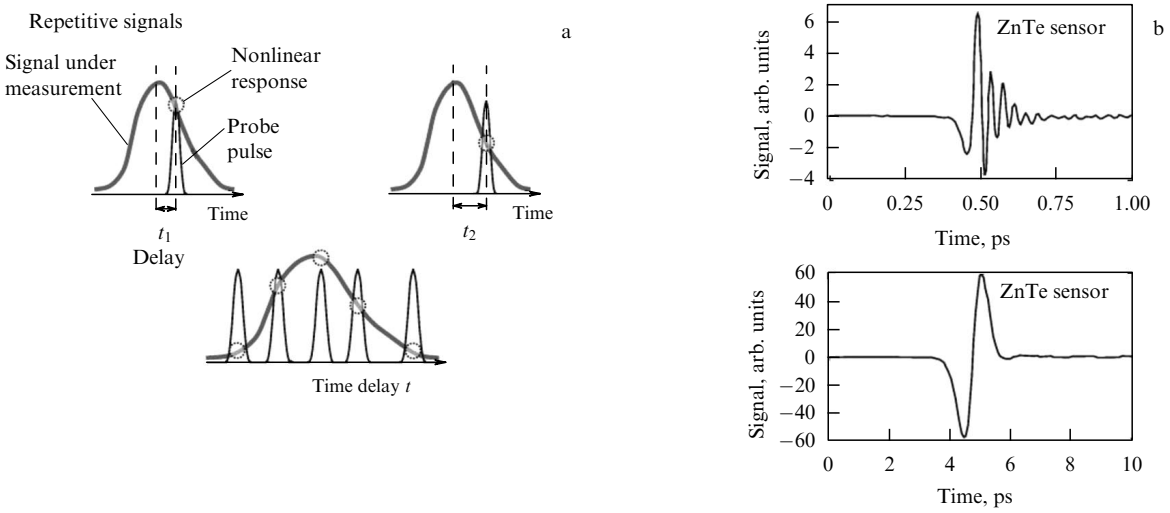

Figure 3. (a) Principle of optical sampling for measuring the waveform of terahertz pulses and (b) examples of measured waveforms with different characteristic time scales.

the resonance magnetic field. That is why these modes experience the strongest coupling to the electrons and the modes with other azimuthal indices are not excited (a strong selection rule).

A large-orbit gyrotron with the particle energy 50–80 keV and a 10–14 T field was developed at the IAP. It selectively generates several modes at the second and third harmonics at the frequencies 0.55–1.0 THz, which are record high for devices of this type, in 8 μs pulses with the peak power 0.3 – 1.8 kW for the pulse repetition rate 0.1 Hz (Fig. 2b) [24]. These devices can operate with relatively low magnetic fields attainable for modern cryomagnetic systems. Presently, a LOG with a lower particle energy (30 keV) and a lower magnetic field (5 T) intended for cw operation at the second, third, and fourth cyclotron harmonics with the output power 3–0.1 kW at frequencies 0.26–0.52 THz is being fabricated at the IAP. With 15 T cryomagnets, which are reasonably affordable at present, it is possible to create similar sources with frequencies up to 1.6 THz.

The limitations on the output power of terahertz gyrotrons related to superhigh field production, the discrimination against parasitic modes in oversized systems, and the ohmic heating of the resonator result in a decrease in the average output power at the fundamental cyclotron resonance to the level of 200–70 kW at frequencies of 0.3–0.5 THz. When operating at the second and third cyclotron harmonics (including the use of LOGs), it will be possible to attain frequencies of 1–1.6 THz with the output power ranging into the kilowatts.

3. Production and detection of coherent broadband terahertz pulses by optoelectronic techniques

The advent and advancement of femtosecond laser technology, which permits obtaining a high peak output power for a moderate average power, underlie the breakthrough in mastering the terahertz range owing to the possibility of using nonlinear effects in various media, both for the generation and for the detection of pulsed coherent broadband radiation. For example, we specify the radiation parameters offered by the Spitfire-Pro laser system used in an IAP facility dedicated to optoelectronics research: the wavelength 0.8 μm, the energy 2–3 mJ in 50 fs pulses, and the pulse repetition rate 1 kHz, corresponding to the peak power 50 GW and the intensity 5–10 GW cm^{-2} in the focusing to a spot with a characteristic size of 100 μm.

The first demonstration experiments on the generation of pulsed free-space terahertz radiation and its detection were carried out in the early 1980s using 'fast' semiconductors (with characteristic photoconductivity rise and decay times lying in the picosecond range) [26] and nonlinear electro-optical crystals [27]. The generation is provided by the rectification (nonlinear detection) of femtosecond laser pulses. As a result, in detecting pulsed terahertz radiation, a unique possibility emerges of measuring the so-called waveform of terahertz pulses, i.e., the temporal dependence of the electric field, which is due to the high repetition rate of the generated terahertz pulses and their high pulse-to-pulse reproducibility. This permits performing 'optical scanning' by varying the delay of optical probe pulses relative to the terahertz pulses that pass through a photoconductor in which the induced voltage is determined by the magnitude and sign of the low-frequency (THz) electric field, or through a nonlinear electrooptical crystal in which the induced birefringence is also determined by the magnitude and the sign of the low-frequency electric field (the linear Pockels effect). Figure 3 outlines the principle of optical sampling for waveform measurements and provides examples of measured waveforms with different characteristic time scales.

The high reproducibility of the generated terahertz pulses is illustrated by the results in Ref. [28] on the phase stabilization of cw radiation in the 100 GHz range, in which high-order harmonics of a terahertz-pulse-repetition frequency (about 100 MHz), clearly resolved for harmonic numbers of the order of several thousand, were used as a reference signal. Using this stabilization system allowed obtaining a record narrow cw radiation line (about 10 Hz at the half-power level).

A comparison of the waveforms of the reference terahertz radiation and the radiation transmitted through samples under investigation underlies numerous applications related to terahertz 'radio-wave imaging' and measurements of the spectra of substances under study in a broad spectral range (so-called time-domain spectroscopy). We emphasize that the Fourier processing of waveforms allows simultaneously

measuring the real and imaginary parts of the permittivity. The detection of terahertz radiation with the use of photodetectors or nonlinear electrooptical crystals, which is well elaborated and commonly accepted presently, is used in a number of commercial devices. At the same time, vigorous studies aimed at a search for new nonlinear materials, new oscillation schemes, the attainment of optimal parameters, as well as fundamental studies are still in progress. Below, we briefly discuss some of them.

In crystals with the group velocity of optical radiation exceeding the phase velocity of terahertz waves, the Cherenkov generation mechanism is possible when a low-frequency pulse of nonlinear polarization of the medium travels at a speed that exceeds the phase velocity of the terahertz radiation. This situation is realized, for instance, in planar sandwich structures developed by the IAP in cooperation with Nizhny Novgorod State University. These structures consist of a glass (BK7) [29] or metal [30] substrate, a nonlinear crystal layer ($LiNbO_3$) several tens of micrometers thick, and a silicon prism. Nonlinear polarization is induced due to rectification of optical radiation in the $LiNbO_3$ layer, and then the Cherenkov terahertz wave wedge passes through the silicon prism; the terahertz radiation is extracted through a bevel prism face. A record high optical-to-terahertz radiation conversion efficiency (of the order of 10^{-3}) was reached. The theoretically expected generation efficiency is higher by about an order of magnitude [31, 32], and the improvement in sandwich structure fabrication therefore gives hope to improve the experimental efficiency. With the use of a metallic substrate, it is also possible to control the spectrum of the terahertz radiation by changing the gap between the nonlinear crystal and the substrate.

Record high values of the terahertz pulse energy (up to 10 μJ), which corresponds to the record high terahertz field intensity (up to 10^7 V cm^{-1} in focusing to a spot 200 μm in diameter), were obtained at the Prokhorov General Physics Institute (GPI), RAS [33]. The generation scheme relies on the optical rectification of high-energy (30 mJ) femtosecond laser pulses with a tilted intensity front propagating through a wide-aperture ($30 \times 30 \times 10$ mm) nonlinear lithium niobate crystal. The tilt angle of the intensity front corresponds to the Cherenkov condition, which substantially increases the time of interaction between the radiated terahertz pulse and the nonlinear low-frequency polarization excited in the medium.

Considerable recent attention has been focused on the plasma mechanisms of terahertz radiation generation involving atmospheric air breakdown induced by focused femtosecond radiation. These generation techniques offer certain advantages over nonlinear rectification in solids: the absence of a 'damage threshold,' allowing the use of arbitrarily high intensities of laser radiation in principle; the absence of clearly defined resonances, which 'cut' appreciable portions from the spectrum of generated terahertz radiation; and a high generation efficiency of several schemes. Furthermore, in remote monitoring systems, it is possible to bring the plasma source and the terahertz radiation detector quite close to the object under inspection. A feature of the modern stage of research on the terahertz radiation generation in a laser-induced spark is that experimental research sometimes takes the lead over the theoretical one and that the theoretical models under consideration often fail to provide a quantitative interpretation of the whole set of experimental data. In this case, one complication arises from the necessity of three-dimensional simulation of the self-consistent dynamics of the focused laser field and the plasma resulting from ionization of the air. Another complication is associated with finding the distribution of low-frequency currents responsible for terahertz radiation; these currents arise from the relaxation of the wave of initial conditions, created at passing a short ionizing optical pulse, in the formed plasma column.

Extensive experimental research into the generation of terahertz radiation in a laser-induced spark was carried out at the dedicated facility at the IAP, which was designed for investigations in the area of optoelectronics. It was shown, in particular, that the imposition of an electric field of about 10 kV cm^{-1} (close to the threshold of air breakdown at atmospheric pressure) increases the generation efficiency by more than a factor of 200 [34] and that the addition of the second harmonic to the optical radiation at a 10% level (with the appropriate phasing of the 1st and 2nd harmonic fields) results in an efficiency increase by more than four orders of magnitude [34, 35]. Furthermore, original findings were reported concerning the radiation pattern and polarization of the terahertz emission from the laser-induced spark, which refute the existing notion that the characteristics of terahertz radiation and the distribution of low-frequency currents in a laser-induced spark, which are responsible for this radiation, are axially symmetric.

Theoretical models were elaborated at the IAP with the specific character of the electron distribution function formation under tunnel ionization in the field of optical radiation taken into account. In the zero-dimensional approximation based on the one-dimensional Boltzmann equation for plasma produced in the process of tunnel ionization, approximate expressions were derived for the source of a quasistationary current; the current excitation efficiency was analyzed for a bichromatic breakdown scheme depending on the laser radiation parameters (the relative phase difference, the polarization, the amplitudes of harmonics) [34–36]. Qualitative agreement was reached between theoretical results and experimental data.

A new mechanism of low-frequency current formation was proposed for laser-induced spark plasmas: in the field (tunnel) ionization of gas in the field of linearly polarized laser radiation, anisotropic pressure emerges in the electron subsystem (with preferential direction along the optical field). In the relaxation of the anisotropy, low-frequency currents are also excited in the direction perpendicular to the optical field, which appreciably changes the radiation pattern and polarization of the terahertz radiation. A numerical code [37] was developed whose application enabled providing a detailed explanation for the formation of a quadrupole radiation pattern of the terahertz radiation and its modification under the application of an external electrostatic field, which was observed in experiments [34].

4. Application of terahertz radiation

In recent years, subterahertz and terahertz sources of coherent radiation have been finding a growing number of various uses. In particular, gyrotrons of the megawatt power level with frequencies up to 0.17 THz are used in the electron–cyclotron heating systems of virtually all modern facilities for controlled fusion (CF) with magnetic plasma confinement. High-stability and relatively low-power gyrotrons are used to substantially improve the sensitivity of high-field NMR spectrometers due to polarization of the paramagnetic subsystem with the subsequent transfer of the polarization state to the nuclear subsystem (dynamic polarization of

nuclei). A cw gyrotron operating at the second harmonic with the radiation frequency 260 GHz and the output power about 100 W [20], recently developed at the IAP, was validly used for this purpose in experiments [38].

A gyrotron with a high working frequency (0.67 THz) and a high pulsed power (300 kW) operating at the main cyclotron resonance has been developed; it is targeted for use in experiments in the remote location of concealed sources of ionizing radiation by the method proposed in Ref. [39]. According to this method, a high-power terahertz wave beam is focused to a small volume, in which the probability of the occurrence of free electrons and of breakdown initiation is low in the absence of ionizing radiation, but is much higher in the presence of ionizing radiation.

At the IAP, a start was made on a feasibility study of making an extreme ultraviolet source with small geometric dimensions ('a point-like source') for high-resolution projection lithography based on the line radiation of multiply charged ions in a discharge induced by terahertz gyrotron radiation. A comprehensive investigation was carried out of self-sustained and initiated discharges maintained by converging terahertz radiation beams in argon and gas mixtures at near-atmospheric pressures [42].

Figure 4 is a schematic representation of the IAP facility intended for obtaining the spectra and images of the specimens under investigation during the passage of terahertz radiation through them. The duration of one scan required to obtain a spectrum in the 0–10 THz frequency interval with the resolution about 1.5 GHz is of the order of 100 s. In demonstration experiments, over one hundred lines of water and carbon sulfoxide in a gaseous state were identified that coincided with the data of well-known catalogs. For example, Fig. 5 shows the 'spectral portraits' of several solvents and proteins in solutions [40]. The two-dimensional radio images of the objects were obtained by point-to-point scanning as the object under study was moved along two transverse coordi-

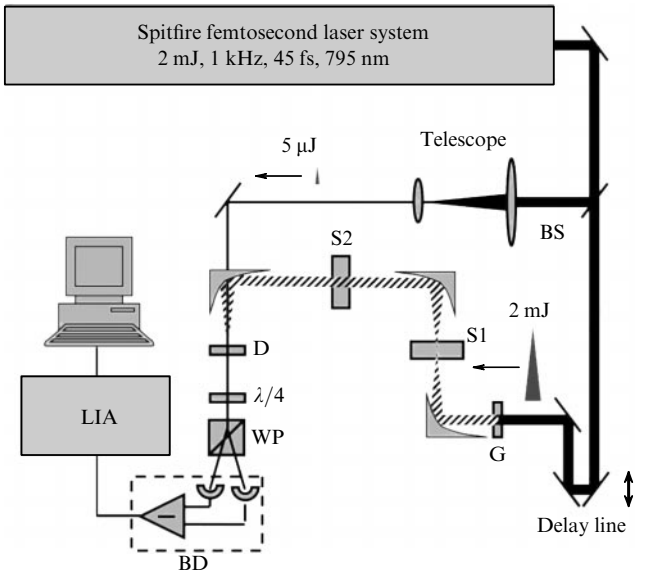

Figure 4. Diagram of the IAP facility designed for optoelectronics research: a delay line makes pulse-to-pulse optical sampling possible, placing a specimen (S1) at the beam waist of terahertz pulses permits obtaining transmission radio images by point-to-point scanning, and placing a uniform specimen in position S2 affords its time-domain spectroscopy. Acoustooptical modulator: BS — beam splitter, WP — Wollaston prism, G — 1 mm ZnTe [110] generator, D — 1 mm ZnTe [110] detector, $\lambda/4$ — quarter-wave plate, S1, S2 — specimens, BD — balanced detectors, LIA — lock-in amplifier. Parameters of a THz pulse: central frequency 0.75–1 THz, spectral width 1–2 THz, duration 0.5–1 ps, field 20 kV cm^{-1}, peak power 3 kW, and conversion efficiency 10^{-6}.

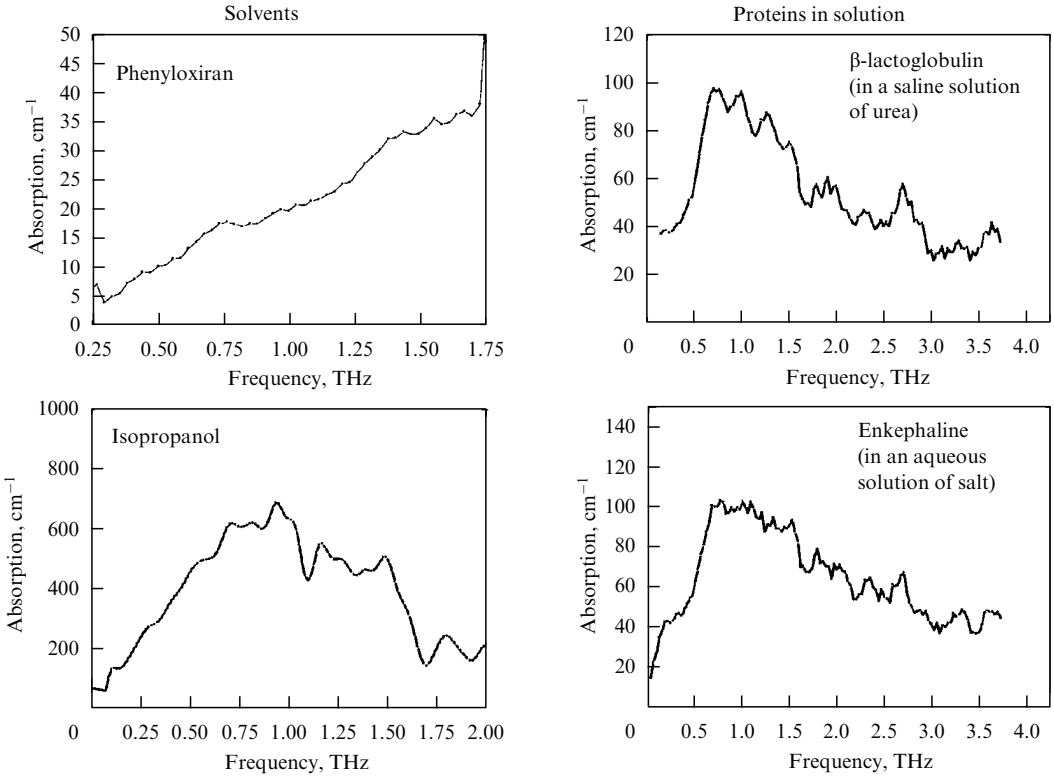

Figure 5. Examples of the 'spectral portraits' of some solvents and proteins in solution.

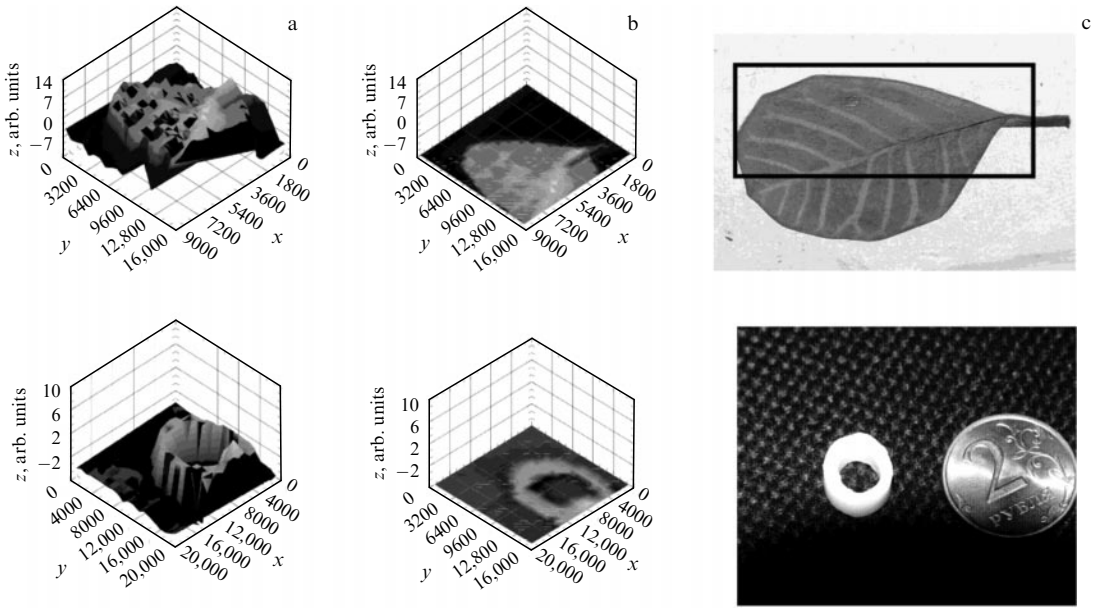

Figure 6. Examples of transmission radio images in the THz range: (a, b) THz radio images for different ways of presentation; (c) optical images.

nates (position S1 in Fig. 4); examples of the images for various ways of presenting the results of processing are given in Fig. 6 [41]. The time taken to obtain one image of an object several square centimeters in size with the resolution about 1×1 mm^2 amounts to almost ten hours under this method, which is suitable only for demonstrations. In this connection, a system presently under development at the IAP is intended for constructing images based on using wide-aperture terahertz beams and high-speed CCD matrices (a CCD is a charge-coupled device). This system will enable obtaining two-dimensional real-time images with a resolution close to the diffraction limit.

One area that shows considerable promise for applications and is under rapid development in many countries is the three-dimensional tomography, which relies on the recording and processing of backscattered terahertz radiation. Among the possible applications, we note the following ones: monitoring of multilayer semiconductor structures during their fabrication, detection of inhomogeneities in stone and concrete structures (flaw detection in new structures and historical monuments, archeology, and so on), investigation of works of art (detection of images concealed under layers deposited later, study of the state of art works prior to their restoration, detection of ancient mural paintings under subsequent layers, including plasterwork), implementation of antiterrorist measures (identification and detection of plastic explosives, toxic agents, and narcotic drugs, inspection of luggage, envelopes, and objects concealed by clothes), and so on. Domestic research in this area is still in its infancy, and its substantial intensification in the near future is called for.

5. Conclusions

At present, the terahertz gap is being efficiently filled both from the side of traditional vacuum electronics and from the side of optoelectronics. Domestic developments in the area of vacuum electronics are at the forefront of the world science. Subterahertz gyrotrons are routinely used in CF facilities with magnetic plasma confinement, as well as in DNP–NMR spectrometers. An output power of $10^2 - 10^4$ W in a pulsed mode has been obtained with relatively compact and accessible gyrotrons with the frequencies up to 1–1.3 THz; cw gyrotrons at the kilowatt power level at the frequencies up to 1 THz are under development. In a short period, domestic femtosecond optoelectronics has been brought up to date in the area involving the quest for new materials, techniques, and oscillation schemes, as well as the demonstration of possible applications. This will permit making the natural transition to the next stage — domestic development of devices for specific applications.

References

1. Tonouchi M *Nature Photon.* **1** 97 (2007)
2. Reimann K *Rep. Prog. Phys.* **70** 1597 (2007)
3. Roskos H G et al. *Laser Photon Rev.* **1** 349 (2007)
4. Humphreys K et al. "Medical applications of terahertz imaging: a review of current technology and potential applications in biomedical engineering" *Conf. Proc. IEEE Eng. Med. Biol. Soc.* **2** 1302 (2004)
5. Knobloch P et al. *Phys. Med. Biol.* **47** 3875 (2002)
6. Hight W A R et al., in *53rd Ohio State Univ. Intern. Symp. on Molecular Spectroscopy* Vol. 53 (1998) p. 158
7. Globus T R et al. *J. Appl. Phys.* **91** 6105 (2002)
8. Belkin M A et al. *IEEE J. Selected Topics Quantum Electron.* **15** 952 (2009)
9. Golant M B, Alekseenko Z T, Korotkova Z S *Prib. Tekh. Eksp.* **12** (3) 231 (1969)
10. Gavrilov N G *Nucl. Instrum. Meth. Phys. Res. A* **575** 54 (2007)
11. Bratman V L et al. *J. Infrared Millimeter Terahertz Waves* **32** 371 (2011)
12. Lysenko E E et al. *Elektromagn. Volny Elektron. Sist.* (11) 63 (2010)
13. Dobbs R et al., in *IEEE Intern. Vacuum Electronics Conf., Monterey, CA, USA* (2010) p. 181
14. Bratman V L et al. *IEEE Trans. Plasma Sci.* **38** 1466 (2010)
15. Zaitsev N I et al. *Radiotekh. Elektron.* **19** 103 (1974)
16. Flyagin V A, Luchinin A G, Nusinovich G S *Int. J. Infrared Millimeter Waves* **4** 629 (1983)
17. Maly T et al. *J. Chem. Phys.* **128** 052211 (2008)
18. Blank M et al., in *Joint 34th Intern. Conf. on IR and MM Waves and 17th Intern. Conf. on Terahertz Electronics, Busan, Korea* (2009) p. W3D02.0112

19. Ogawa I et al., in *Joint 34th Intern. Conf. on IR and MM Waves and 17th Intern. Conf. on Terahertz Electronics, Busan, Korea* (2009) p. W3D03.0309
20. Zapevalov V E et al., in *Joint 34th Intern. Conf. on IR and MM Waves and 17th Intern. Conf. on Terahertz Electronics, Busan, Korea* (2009) p. W3D04.0389
21. Saito T et al. *Int. J. Infrared Millimeter Waves* **28** 1063 (2007)
22. Glyavin M Yu, Luchinin A G, Golubiatnikov G Yu *Phys. Rev. Lett.* **100** 015101 (2008)
23. Idehara T et al. *Int. J. Infrared Millimeter Waves* **29** 131 (2008)
24. Bratman V L, Kalynov Yu K, Manuilov V N *Phys. Rev. Lett.* **102** 245101 (2009)
25. Denisov G G et al. *Nucl. Fusion* **48** 054007 (2008)
26. Auston D H, Cheung K P, Smith P R *Appl. Phys. Lett.* **45** 284 (1984)
27. Valdmanis J A, Mourou G, Gabel C W *Appl. Phys. Lett.* **41** 211 (1982)
28. Tretyakov M Yu et al. *Pis'ma Zh. Eksp. Teor. Fiz.* **91** 240 (2010) [*JETP Lett.* **91** 222 (2010)]
29. Bodrov S B et al. *Opt. Express* **17** 1871 (2009)
30. Suvorov E V et al., in *Strong Microwaves: Sources and Applications: Proc. of the VII Intern. Workshop, Nizhnii Novgorod, 27 July – 2 August 2008* Vol. 2 (Ed. A G Litvak) (Nizhnii Novgorod: Russian Academy of Sciences, Institute of Applied Physics, 2009) p. 529
31. Bodrov S B et al., in *Sbornik Trudov Mezhdunarodnogo Opticheskogo Kongressa "Optika — XXI vek"* (Proc. of the Intern. Optical Congress — XXI Century) (Eds V G Bespalov, S A Kozlov) (St. Petersburg: SPbGU ITMO, 2008) p. 298
32. Bakunov M I, Bodrov S B *Appl. Phys. B* **98** 1 (2010)
33. Garnov S V, Shcherbakov I A *Usp. Fiz. Nauk* **181** 97 (2011) [*Phys. Usp.* **54** 91 (2011)]
34. Akhmedzhanov R A et al. *Izv. Vyssh. Uchebn. Zaved. Radiofiz.* **52** 536 (2009) [*Radiophys. Quantum Electron.* **52** 482 (2009)]
35. Akhmedzhanov R A et al. *Zh. Eksp. Teor. Fiz.* **136** 431 (2009) [*JETP* **109** 370 (2009)]
36. Fadeev D A, Mironov V A *Opt. Zh.* **77** (10) 32 (2010) [*J. Opt. Technol.* **77** 615 (2010)]
37. Zharova N A, Mironov V A, Fadeev D A *Phys. Rev. E* **82** 056409 (2010)
38. Denysenkov V et al. *Phys. Chem. Chem. Phys.* **12** 5786 (2010)
39. Granatstein V L, Nusinovich G S *J. Appl. Phys.* **108** 063304 (2010)
40. Akhmedzhanov R A et al. *Izv. Vyssh. Uchebn. Zaved. Radiofiz.* **48** 939 (2005) [*Radiophys. Quantum Electron.* **48** 837 (2009)]
41. Akhmedzhanov R A, Ilyakov I E, Shishkin B V, in *Nelineinye Volny — 2006* (Nonlinear Waves — 2006) (Executive Eds A V Gaponov-Grekhov, V I Nekorkin) (Nizhny Novgorod: Institut Prikladnoi Fiziki RAN, 2007)
42. Bratman V L et al. *Phys. Plasmas* **18** 083507 (2011)

PACS numbers: **03.75.–b**, **37.10.–x**, **67.85.–d**
DOI: 10.3367/UFNe.0181.201108g.0875

Ultracold atoms and atomic optics

V I Balykin

1. Introduction

As a quantum mechanical system, the atom is characterized by two sets of degrees of freedom: internal (electron configurations and spin) and external (momentum and center-of-mass position), which can change in the interaction with laser radiation. The physics of ultracold atoms and atom optics made their appearance due to successful investigations into the action of laser radiation on precisely the external degrees of freedom of the atom — its momentum and center-of-mass position. In an elementary 'photon absorption–emission' cycle, the reradiated photon can be spontaneous or induced. The 'stimulated absorption–spontaneous emission' process is inherently dissipative and it is precisely this cycle that underlies the laser cooling of atoms. Numerous laser cooling techniques enable forming atomic ensembles in the range from room temperature to several nanokelvins. Laser cooling and the subsequent evaporative cooling allow obtaining both ultralow temperatures and ultrahigh atomic densities, which in turn permits realizing quantum Bose and Fermi gases. The 'stimulated absorption–stimulated emission' photon process is coherent and forms the foundation of atom optics — a new type of optics of material particles (along with electron and neutron optics), which evolved from the development of the methods of laser cooling and atom localization and which is concerned with the formation, control, and application of the ensembles and beams of neutral atoms.

V I Balykin Institute of Spectroscopy, Russian Academy of Sciences, Troitsk, Moscow region, Russian Federation
E-mail: balykin@isan.troitsk.ru

Uspekhi Fizicheskikh Nauk **181** (8) 875–884 (2011)
DOI: 10.3367/UFNr.0181.201108g.0875
Translated by E N Ragozin; edited by A M Semikhatov

2. Laser cooling of atoms

It is common knowledge that one of the main properties of laser radiation is its extremely high effective temperature, which exceeds the solar temperature by many orders of magnitude, even for low-power lasers. This unique property of laser radiation sharply distinguishes it from the light emitted by conventional thermal sources. Owing to this property, laser radiation has gained wide acceptance in thermal material processing. Also considered is its application for the initiation of thermonuclear reactions.

Not immediately evident is the idea of cooling substances by laser light. On the face of it, this seems to be hardly compatible. Nevertheless, not only has it been proved in the past 20 years that lasers can cool atoms moving freely in a low-pressure gas or in an atomic beam, but a new area of research has also emerged — the physics of ultracold atoms. The minimal temperatures attainable presently are as low as several nanokelvins.

The laser cooling of an ensemble of atoms occurs in the resonance or quasiresonance energy and momentum exchange between the atoms and laser radiation. The energy of the atomic ensemble then decreases and the radiation energy increases. Three laser cooling mechanisms are known, which are referred to as Doppler, sub-Doppler, and subrecoil mechanisms.

2.1 Doppler cooling

In the interaction of an immobile atom with monochromatic laser radiation of frequency ν_L, the atom absorbs a resonance photon ($\hbar\nu_L = \hbar\nu_0$, where ν_0 is the optical transition frequency) and experiences a transition from the ground state to an excited one. The photon absorption changes the atomic velocity by the value of the recoil velocity $v_{ret} = \hbar k/M$, where $\hbar$ is the Planck constant, $k = 2\pi/\lambda$ is the wave vector, λ is the radiation wavelength, and M is the atomic mass. The atom can return from the excited state to the initial one with the stimulated or spontaneous emission of a photon. In the stimulated emission, the photon has the same energy and propagation direction as the absorbed photon, resulting in the reverse change of the atomic velocity by v_{ret}. In

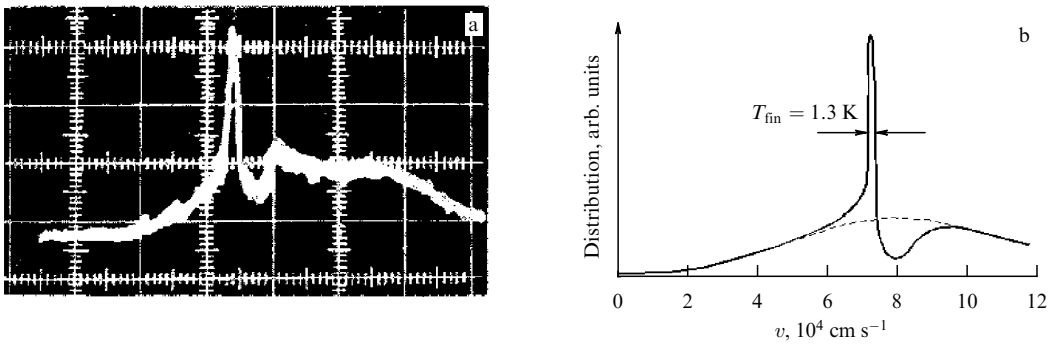

Figure 1. First experiment on the laser cooling of neutral atoms. (a) Experimental profile of the velocity distribution of an atomic sodium beam after its laser irradiation. The cooled atoms form a narrow velocity group with the temperature 1.5 K. (b) Calculated dependence.

the spontaneous emission, the photon has an arbitrary propagation direction, and therefore the average contribution of such photons to the variation of atomic velocity and momentum is equal to zero. On average, the photon momentum is therefore transferred to the atom in the stimulated absorption followed by the spontaneous emission of a photon. As a result, when an atom interacts with light of the resonance frequency, it experiences light pressure in the direction of the laser beam propagation.

The resonance between the frequency of laser light and the atomic absorption frequency is extremely narrow owing to the small width of atomic absorption lines. Consequently, if the frequency of laser light is changed by the width of an absorption line, the atom does not undergo excitation and the force of light pressure sharply decreases in magnitude. In the case of a moving atom, the resonance between monochromatic laser radiation and the atom shifts due to the Doppler shift, and the light pressure experienced by the atom is highest at the resonance velocity $v_{\text{res}} = (\nu_{\text{L}} - \nu_0)/\lambda$. For $\nu_{\text{L}} > \nu_0$, the resonance emerges when the atom is moving in the propagation direction of the laser beam; for $\nu_{\text{L}} < \nu_0$, the resonance emerges when the atom is moving in the opposite direction to the beam. Therefore, the force of light pressure of monochromatic radiation is a selective function of the atomic velocity, and the atom experiences the force of light pressure when the direction and magnitude of its velocity satisfy the resonance condition.

Under a multiple repetition of the photon absorption–emission cycle, the atomic momentum changes by $\Delta p = N\hbar k$, where N is the number of cycles. When the direction of atomic motion is opposite to the direction of the laser beam, the atom decelerates. For instance, for a sodium atom, which has the velocity about 10^5 cm s^{-1} at room temperature and the recoil velocity $v_{\text{ret}} = 3$ cm s^{-1}, the velocity of the atom is reduced to virtually zero after approximately 10^4 'absorption–spontaneous emission' cycles.

When an atom decelerates under the action of laser radiation, a Doppler shift emerges between the atomic absorption frequency and the laser radiation frequency, with the consequential decrease in the efficiency of reradiation of laser photons by the atom and, accordingly, of the atomic deceleration efficiency. The Doppler shift is eliminated by changing the laser radiation frequency or the atom transition frequency (for instance, in a magnetic field) in the course of deceleration of the atom. When permanent resonance is maintained between the atom transition frequency and the radiation frequency, deceleration of all atoms with the velocity equal to the velocity projection occurs in the direction of the laser beam. The application of three pairs of mutually perpendicular counter-propagating laser beams allows decreasing all velocity components of the atoms, i.e., realizing three-dimensional cooling of the atomic gas. This kind of laser cooling is known as the *Doppler cooling*.

The idea of laser cooling of neutral atoms was first introduced by Hänsch and Schawlow in 1975 [1]. The first experiments on the laser cooling of atoms were carried out at the Institute of Spectroscopy, RAS (ISAN) [2] (Fig. 1) using a sodium atomic beam. A collimated beam of sodium atoms was irradiated by a counter laser beam with a frequency lying within the Doppler profile of the absorption line. Because the laser radiation spectrum was much narrower than the Doppler width, efficient deceleration was experienced only by the atomic fraction that was at resonance with the radiation field. The velocities of the remaining atoms were only slightly changed. The deceleration of atoms continued until they went out of resonance with the radiation due to the emergence of a Doppler shift. The decelerated atoms formed a narrow velocity cluster. Because the temperature in an ensemble of atoms is defined by their velocity spread, knowing the velocity distribution allows determining the temperature of the atomic ensemble. In the first experiments with sodium atoms (see Fig. 1), the temperature was decreased from 1000 K to 1.5 K [2]. In the subsequent experiment on transverse cooling of an atomic beam at the ISAN, a temperature of 35 mK was attained.

The photon absorption and emission by an atom are inherently random in time and direction, resulting in a random variation of atomic momentum and an increase in its rms value and in the heating of an atomic ensemble. The lowest atomic temperature in the Doppler cooling is determined by the equilibrium between laser cooling and the heating due to momentum diffusion under spontaneous atomic transitions. The lowest atomic temperature in the Doppler laser cooling is $k_{\text{B}} T_{\text{Doppler}} \approx \hbar\Gamma$, where Γ is the width of the excited atomic level. The Doppler temperature is typically about 100 μK. This is the so-called *Doppler limit* for laser cooling of atoms; its magnitude was first determined by Minogin and Letokhov [3].

One of the most important consequences of the first experiments on laser cooling of atoms was the possibility of their localization under different configurations of electric, magnetic, and laser fields [4]. The localization of atoms opened the way to different methods of laser cooling, whose

application allowed a further decrease in the atomic temperature.

2.2 Sub-Doppler cooling

For a long time, the Doppler limit of atomic temperature was regarded as the fundamental limit decreasing the temperature below which was impossible in principle. In 1988, in experiments with Na atoms localized in a magnetooptical trap (MOT), W Phillips's group of the National Institute of Standards and Technology (NIST), USA, unexpectedly recorded an atomic temperature substantially lower than the Doppler temperature limit [5]. It was not long before an explanation for the cooling to temperatures below the Doppler limit was provided.

As noted in the Introduction, atomic particles are characterized by internal (electron configuration, spin) as well as external (momentum and center-of-mass position) degrees of freedom. A strong correlation between the dynamics of the internal and external degrees of freedom underlies the laser cooling to below-Doppler-limit temperatures. In the Doppler laser cooling, an atom is assumed to be a nondegenerate two-level quantum system, and the laser field is assumed to be spatially uniform and unpolarized. When the states of the atom are multilevel and degenerate in Zeeman sublevels while the laser beams make up a nonuniform field distribution with polarization varying periodically in space, the atom finds itself in a periodic potential depending on the magnetic sublevel. When moving in this potential field, the atom periodically rises and descends between the potential peaks and valleys, converting its potential energy into kinetic energy and vice versa. If the frequency of the laser field is taken to be lower than the atomic transition frequency, then the atom is more likely to absorb a laser photon at the peak of the potential and, on emitting a spontaneous photon, transit to another magnetic sublevel, at which the potential energy of the atom is minimum. The difference in potential energy is carried away by the spontaneously emitted photon, with the consequential decrease in the kinetic energy of the atom and cooling in the atomic ensemble. This mechanism of laser cooling was called the *sub-Doppler cooling*. The lowest atomic temperature for sub-Doppler cooling is determined by the photon recoil energy and is about 1 μK for alkali atoms.

2.3 Subrecoil cooling

In the majority of laser cooling systems, the 'stimulated absorption–spontaneous photon emission' cycle never terminates. Because the momentum $\hbar k$ transferred to an atom by a spontaneously emitted photon is random in time and direction, it seems that there is no way to decrease the spread of atomic momentum δp below the photon momentum $\hbar k$. But this fundamental limitation on the atomic temperature has also been overcome. The main idea of subrecoil laser cooling is to make a small domain around the zero atomic velocity in the momentum space where the probability of photon absorption and the rate of spontaneous photon reradiation tend to zero. If this strategy is implemented successfully, the atom in the laser field 'wanders' in the momentum space when executing the 'stimulated absorption–spontaneous photon emission' cycles and may acquire a velocity close to $v = 0$, whereby it no longer absorbs photons and is protected from the detrimental influence of light. By selecting special configurations of the laser field defined by the type of atoms and their interaction conditions, it is possible to make a small domain where the photon absorption probability and the spontaneous photon reradiation rate tend to zero.

There are two methods of laser cooling below the single-photon recoil level: *Raman* cooling and cooling based on *velocity-selective coherent population trapping* (VSCPT).

In *Raman* cooling, a two-photon transition between two hyperfine structure components of the ground state of an atom is used. The atom is irradiated by two laser pulses. When the frequencies of the pulses differ by the hyperfine splitting of the atomic ground state and are far away from the domain of single-photon resonances, the atom goes over from one state of the hyperfine structure to another due to a two-photon Raman event. Raman transitions are insensitive to the Doppler shift in the configuration of unidirectional laser beams. In the configuration of oppositely directed laser beams, the Doppler shifts add up and the atomic resonance with the field depends on the atomic velocity. The width of the resonance is extremely narrow and is typically determined only by the atom–field interaction time. This, in turn, signifies that it is possible to selectively excite very narrow velocity groups of atoms. When the frequency difference is offset to the red side of the spectrum relative to the frequency of the two-photon resonance, an atom traveling with a positive velocity is at resonance with the field due to the Doppler shift and acquires a momentum such that its velocity decreases. By using a sequence of varied-frequency pulse pairs with varying directions of the laser beams, it is possible to increase the density of atoms with nearly zero velocities. The temperature thus reached is about 100 nK, which corresponds to 1/10 of the recoil energy. Raman cooling was first observed at Stanford University, USA (S Chu) [6].

In another method of subrecoil atom cooling, the effect of velocity-selective coherent atomic population trapping is used. The heart of the method is as follows: in the course of interaction with laser radiation, atoms are transferred to a state that is a superposition of sublevels of the ground atomic state, wherein atoms no longer interact with the radiation. The interaction vanishes owing to the destructive interference of the amplitudes of absorption in the atomic transition from sublevels of the ground state to the excited state. The absorption suppression is velocity selective, and the absorption becomes zero for those atoms that reach zero velocity as a result of random walk in the momentum space [7].

With advances in laser cooling techniques and the subsequent confinement of atoms in traps, it became possible to reach subrecoil atomic temperatures by using only one cooling technique, the Doppler one. The cooling proceeds in two stages. Doppler cooling is accomplished at the first stage with the use of *allowed* atomic transitions; at the second stage, Doppler cooling with a *forbidden* transition is used.

Therefore, the use of combinations of different laser techniques for cooling and trapping neutral atoms presently enables lowering the temperature of atomic ensembles from about 1000 K to 10 nK, i.e., by eleven orders of magnitude. Figure 2 shows the main physical mechanisms of laser cooling of neutral atoms. The initial atomic ensemble is an atomic gas or an atomic beam at near-room temperature. Doppler cooling permits decreasing the atomic temperature to about 1 mK (cold atoms). The localization of atoms in different electromagnetic traps and their further cooling by laser sub-Doppler techniques to temperatures about 1 μK (ultracold

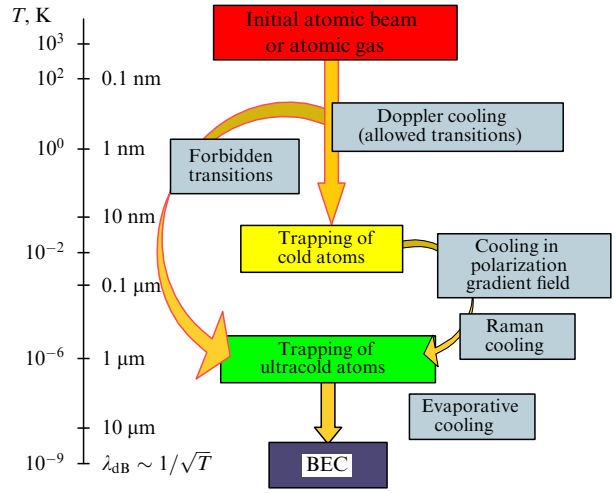

Figure 2. Principal physical mechanisms of laser cooling of neutral atoms.

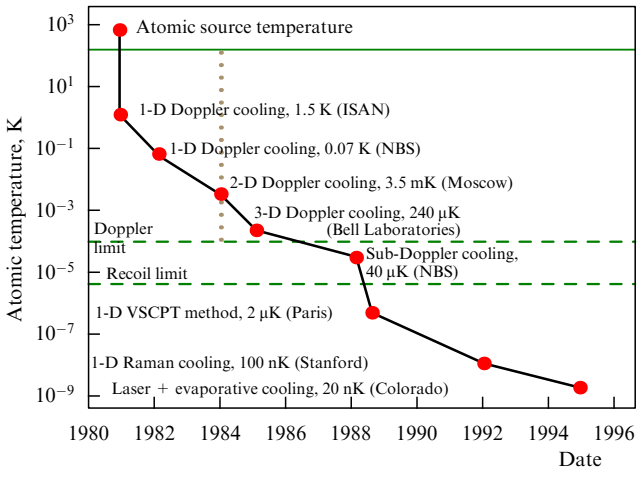

Figure 3. Progress in the laser cooling of atoms (the key experiments), which traces back to the work carried out at the Institute of Spectroscopy, RAS, in 1981. (NBS: National Bureau of Standards, USA).

atoms) are made possible at these temperatures. Evaporative cooling allows additionally decreasing the temperature of the atomic ensemble to about 100 nK with a simultaneous increase in the atomic phase density, which permits realizing the Bose–Einstein condensation (BEC) of the atoms. Ultracold atoms can also be obtained from cold atoms in the Doppler cooling using forbidden transitions.

Figure 3 is representative of the progress in the laser cooling of atoms (the key experiments), which traces back to the work carried out at the ISAN in 1981.

In 1997, S Chu, W Phillips, and C Cohen-Tannoudji were awarded a Nobel Prize in physics for development of methods to cool and trap atoms with laser light.

2.4 Localization of atoms

One of the fundamental physical problems, apart from the cooling of atoms, is their confinement in a bounded spatial domain — in a trap. The laser cooling of atoms allowed the localization of atoms under different configurations of electric, magnetic, and laser fields. Three approaches to atom localization were developed, which rely on the use of magnetic fields, laser fields, and a combination of laser, magnetic, and gravitational fields [4].

In a *magnetic trap* (first realized in [8]), atoms are confined by a nonuniform stationary magnetic field. In this field, an atom with a permanent magnetic moment experiences a force directed to the minimum of the magnetic field for the required orientation of the atomic moment; the atoms are localized at the field minimum. One of the versions of a magnetic trap is a spherical quadrupole magnetic trap, in which two oppositely directed circular currents induce a static magnetic field in the form of a spherical quadrupole. The magnetic field increases from the trap center toward its edge and therefore forms a potential well for atoms with a negative projection of the magnetic moment on the field direction. For an atomic magnetic moment approximately equal to the Bohr magneton and a moderate magnetic field at the trap edges (about 100 G), this trap is capable of confining atoms with the temperature about 10 mK.

Localization in optical fields is based on the action of the dipole radiation force. The simplest optical trap for cool atoms consists of only one focused laser beam. The dipole force of light pressure, which acts on an atom in a laser beam, forms a three-dimensional potential well near the focus of the laser beam for a negative laser frequency detuning relative to the frequency of the atomic transition. The properties of this optical trap, which is referred to as the dipole trap, depend on the magnitude of this frequency offset and the laser radiation intensity. The depth of this potential well may be 0.1–1 mK and the atom lifetime in the dipole trap may range from several tens of milliseconds to approximately 10 min [9], depending on these parameters.

The simultaneous use of static magnetic fields and laser beams makes the *magnetooptical trapping* of atoms possible. The force of light pressure on an atom in this trap is equal to the sum of two forces: the friction force and the harmonic restoring force, which permits the atoms to be cooled and localized. In a magnetooptical trap, the temperature of the atomic cloud ranges between 1 mK and 10 μK, the atom density is $10^8 - 10^{12}$ cm^{-3}, and the trap depth is 1 K, which is far greater than in purely magnetic and laser traps. Such a trap was first implemented by Raab et al. [10]. This trap permits localizing isotopes of lithium, sodium, potassium, rubidium, cesium, and francium and atomic isotopes of alkaline-earth elements, calcium, strontium, and rare-gas isotopes.

One more method that has been developed for trapping cool atoms relies on the combined use of electromagnetic and gravitational forces. The conceptually simplest *gravitational–optical atom cavity trap* may consist of only one horizontally arranged concave laser mirror for atoms [11, 12]. In this geometry, the function of the second spatially distributed mirror is fulfilled by the gravitational field.

2.5 Evaporative cooling

Evaporation — the conversion of matter from the liquid state to the gaseous state — is a well-known physical phenomenon. In the course of evaporation, particles with energies exceeding the binding energy escape from the particle ensemble, and this depletion of the ensemble in high-energy particles leads to its cooling. Evaporative cooling is a universal process inherent in the microworld (evaporation of a neutron from a nucleus) as well as in the macroworld (evaporation of stars from stellar clusters).

The evaporative cooling of neutral atoms preliminarily localized in electromagnetic traps permitted obtaining low temperatures, down to 10 nK [13]. The procedure for obtaining these low temperatures has several stages. First, atomic ensembles are preliminarily cooled by laser cooling to temperatures at which their localization in electromagnetic traps is possible. The next step is evaporative cooling. The main prerequisites for the evaporative cooling are a sufficiently long atomic lifetime in the trap and a sufficiently high atom density for the onset of efficient cooling. The atomic lifetime in the trap is limited by inelastic atomic collisions ('bad' collisions). On the other hand, elastic ('good') atomic collisions are needed to thermalize the atomic ensemble. Realizing atomic evaporative cooling requires the thermalization time to be shorter than the atomic lifetime in the trap.

A significant disadvantage of evaporative cooling is the loss of a large fraction of atoms, up to 0.1%. But the evaporative cooling transforms ensembles with a large number of atoms to high-density low-temperature ensembles, i.e., to ensembles with a high phase density. It is the attainment of a high phase density in the evaporative cooling of atoms that has allowed implementing Bose–Einstein condensation of atoms [14, 15] and quantum Fermi gases [16, 17].

3. Atom optics

Atom optics, along with electron, ion, and neutron optics, is the optics of material particles concerned with the formation of ensembles and beams of neutral atoms, controlling them, and applying them to basic research and practical uses [18–22]. Atom optics came into being as a physical discipline in its own right in the mid-1990s as a result of investigations into the action of the forces of light pressure on the translational motion of atoms.

The advancement of atom optics is intimately related to the development of the techniques of laser cooling and localization of neutral atoms. The laser cooling of atoms and their localization allow forming atomic ensembles and beams with prescribed parameters and decreasing the atomic temperature to only one millionth of a degree above absolute zero. At these temperatures, the atomic de Broglie wavelength is comparable to the wavelength of light and the wave properties of atoms make themselves evident.

The potential of atom optics is substantially greater than for other types of material particle optics (electron and neutron optics) due to the existence of the internal atomic structure. The wavelengths and the types of interactions relevant to the different types of optics are indicated in Table 1.

Table 1.

Type of optics	Wavelength range, m	Interaction types
Photon optics	$10^{-5}-10^{-11}$	Light with matter
Charged-particle optics	$10^{-10}-10^{-11}$ (electrons) $10^{-13}-10^{-14}$ (ions)	Electrons and ions with electric and magnetic fields
Neutron optics	$10^{-7}-10^{-10}$	Neutrons with nuclei
Atom optics	$10^{-5}-10^{-11}$	Atoms with laser, electric, and magnetic fields

For a temperature close to absolute zero, when the de Broglie wavelength is comparable to the interatomic distance, the behavior of an atomic ensemble is markedly affected by an internal quantum characteristic of an atom, its spin. The striking difference between the behavior of fermions and bosons is observed at very low temperatures: Bose–Einstein condensation is observed for Bose particles. The first atomic condensates were obtained by several groups of American physicists with the use of laser and evaporative cooling of atoms in 1995 [14, 15]. A magnetic trap that confines BEC atoms is an analog of an optical resonator for photons in an optical laser. The atoms that can 'emanate' from a magnetic trap in a specific direction (like photons through the semitransparent mirror of an optical laser resonator) make up a coherent directional beam, which is similar to a laser beam. This device was given the title 'atom laser' [23, 24]. The keen interest in atom lasers is due to the prospect of applying coherent atomic beams in high-precision measuring instruments and high technologies in the fabrication of atomic and molecular nanostructures.

We consider only two of the numerous fields of research in atom optics: atomic interferometry and atomic nanolithography.

3.1 Sources in atom optics

In light optics, an ideal source for both basic research and applied problems is the laser: its radiation has a long coherence length, is highly collimated, and provides a high-intensity photon flux in the beam. In atom optics, there are two main source types: thermal atomic beams and the beams from cool and localized atomic ensembles. Both source types find application, but just the development of laser techniques for the cooling of atoms and their confinement has allowed creating atomic sources with a high phase density. One of the decisive prerequisites for the successful development and application of atomic interferometry and atomic nanolithography is the use of atomic sources with a high phase density.

3.2 Atomic interferometry

Since the early 20th century, studies of the wave behavior of light, including the capacity of waves for interference, have been an important area of physics. During the past century, light interferometers have come to be the most precise measuring devices, finding use in both basic research and numerous applications.

De Broglie's and Schrödinger's initial idea that moving particles are waves has led to the advent of electron and neutron interferometers, and in the last decade of the 20th century, in connection with the development of the methods of laser cooling and confinement of atoms, to the advent of atomic interferometry [25, 26]. Atom interferometers offer several advantages over their electron and neutron counterparts. First, the parameters of atomic particles (mass, magnetic moment, polarizability) occupy a wide range of values; accordingly, the force of interaction of atoms with an external field may vary by many orders of magnitude, depending on the type of atoms selected. Second, both internal and external degrees of freedom of an atom can be efficiently controlled by laser radiation because the light scattering cross section for an atom is about 10^{-9} cm^2, while that for the electron is only 10^{-25} cm^2. Third, the frequency and wavelength of laser radiation are presently measured with a very high precision, 10^{-15} and 10^{-11}, which predetermines a

higher accuracy of measurements with atom interferometers than with the electron and neutron ones. Lastly, atom sources are relatively simple and inexpensive compared to electron and neutron sources.

The implementation of an atom interferometer involves the creation of the following elements: an atom source, a coherent splitter of atomic de Broglie waves, mirrors for the recombination of the waves, and an interference pattern detector.

The simplest *atomic source* is an atomic beam formed by two collimating slits. A disadvantage of this source is its low phase density, and the important advantage of using a thermal beam in interferometry — its initially high atom flux — is therefore lost. A source prepared by laser cooling and subsequent trapping of atoms in electromagnetic traps is preferable.

The next step in the making of an atom interferometer is the coherent *splitting* of an atomic wave. One splitting technique relies (by analogy with that in optics) on the effect of diffraction of atoms. To realize diffraction, material nanogratings and light gratings are used. A disadvantage of the former is that a significant fraction of the incident atomic beam is blocked. Light gratings, which are a standing wave, i.e., are phase gratings, transmit all of the atoms and therefore turn out to be higher in efficiency for atom interferometers.

Another technique for the coherent splitting of an atomic wave is based on the possibility of coherent superposition of two atomic states in momentum space. This coherent superposition is produced by irradiating atoms with resonance laser radiation. In this case, a coherent superposition of internal degrees of freedom of the atom — its ground and excited states — occurs. These internal states also differ by their translational momentum, equal to the photon momentum. If the initial momentum state of the atomic ensemble is well localized, the components of the atomic wave function become spatially separated with time.

Observing an interference pattern requires arranging a *recombination* of two atomic waves. In an atom interferometer, as in an optical one, the recombination is effected involving *atom mirrors*. The reflection of atoms from a surface light wave was the first demonstration of the atom mirror [27]. This wave, when spatially modulated, can also serve as a coherent splitter of an atomic beam. The role of an atom mirror can also be played by a laser beam. In this case, an atom undergoes a transition to an excited state on absorbing a laser photon, which in turn leads to its deflection by the angle determined by the momentum of the absorbed photon.

Recombination of atomic beams can be realized (like their splitting) by using the effect of atom diffraction from material nanogratings or standing light waves. The first experiments were carried out using precisely diffraction for both the splitting and the recombination of atomic beams [25, 26].

Interference fringes in an atom interferometer can be observed as the oscillations of the atomic beam intensity directly in space with the help of a *coordinate-sensitive detector*. Another way of observing interference involves transfer of information from the wave function phase to the populations of internal atomic states. This is achieved in the recombination of wave-function components by laser pulses. The subsequent application of an *internal-state-selective detector* of atoms enables detecting oscillation of the atomic beam intensity at the interferometer output as a function of the phase difference.

The scheme of an atom interferometer based on laser pulses is most common today. It is pertinent to note that so 'simple' a control over the atom had never been possible until the development of methods for laser cooling and the trapping of atoms, which allowed producing slow atomic beams and beams with a narrow velocity distribution. The first circumstance permits the atom of a beam to be appreciably deflected even on transferring the momentum of a single photon to the atom, and the second circumstance permits separating the beams in space.

The major significance of atomic interferometry for basic research and numerous applications lies in the fact that it is possible to measure phase shifts induced by extremely low potentials. For instance, a beam of sodium atoms acquires a phase shift of about 1 rad for the potential of 6×10^{-12} eV and the interaction length of 10 cm. The measurement of a 10^{-3} rad phase shift corresponds to the measurement of potential with the relative precision $\approx 10^{-14}$. When cold atoms are used, the precision of measurements additionally increases by a factor of 1000. With atom interferometers, it has been possible to carry out superhigh-accuracy measurements of rotation (gyroscopes), Earth's gravitational field, atomic polarizability, the fine structure constant, and atom–surface interactions. The precision of these measurements greatly exceeds that of previous methods [26].

Phase shifts in an atom interferometer are subdivided into four types: (i) dynamic, (ii) topological, (iii) gravitational, and (iv) inertial (the last two are caused by gravitational and inertial forces). In a potential field, where the energy of an atom depends on its coordinate, the atom experiences a force, which determines its dynamics. From the dynamics, it is possible to decide about the magnitude and character of the field; in other words, the atom plays the role of a test body. An alternative possibility for extracting information about the field is provided by interference measurements, in which the phase increase of the atomic wave function is determined by the nature and magnitude of the potential. In such fields, the phase shift is termed dynamic.

Atomic interferometry allows investigating physical fields that are independent of spatial coordinates, when the field gradient and, accordingly, the force experienced by an atom in the field are equal to zero. Such a field is not detectable by classical methods involving particle trajectory measurements. It can nevertheless be discovered and investigated by atomic interferometry techniques, because the phase of the wave function changes in the motion of the atom in the field. The phase shift in such fields is referred to as *topological*. The best-known examples of the topological phase shift are the Berry phase and the phases in the Aharonov–Bohm and Aharonov–Cashier effects.

Among the most impressive applications of atomic interferometry is decoherence research [28]. Quantum systems can be in the state of coherent superposition of many states. Interactions with the environment are responsible for the coherence breakdown of the states. This effect is known as 'decoherence.' Research into decoherence and the ways to suppress, correct, and control it is central to the area of quantum informatics, the development of quantum computers, and nanotechnology [29–31]. A quantum computer can be perceived as a complicated interference device that performs operations on superposition (and coherent) states. The coupling to the environment, arising due to decoherence, its rate and the capability of controlling it underlie the success of operation of the quantum computer.

Because the operation of an atom interferometer is based on the coherence of atomic ensembles in use and its constituent elements (source, splitter, mirrors), it is sensitive to the processes that disrupt coherence. Numerous experiments have been carried out to investigate the loss of coherence due to coupling to the environment (spontaneous photon reradiation in the transit of an atom through the interferometer), during the procedure of acquiring the information as to which interferometer arm the atom is flying through, etc. [25, 26].

An atom interferometer opens outstanding possibilities of verifying fundamental physical laws. *Verification of the charge neutrality* of the atom (the charge equality of the electron and the proton, the neutrality of the neutron) is of significance for the fundamental particle theory. The experimental neutrality test for a macroscopic amount of substance sets a limit on the accuracy of the electron and proton charge equality: $(q_p + q_e)/e < 10^{-21}$. It has been theoretically shown that atomic interferometry is able to improve the measurement accuracy to 10^{-22}.

The *Newton constant G* in the law of universal gravitation $V(r) = Gm_1m_2/r$ is among the fundamental constants measured with the lowest accuracy. Its relative accuracy is 1.4×10^{-4}. Atomic interferometry is a relatively new method of determining this constant, but even in the first measurements performed by atomic interferometry [26], it was possible to achieve an accuracy of 3×10^{-3}. Experiments to measure G with an accuracy of 10^{-4} are planned for the future.

The effort of the physical scientific community to *unify the description of all known types of interaction* (strong, electromagnetic, weak, and gravitational) leads to the model of the interaction of two masses that differs from the Newtonian law of universal gravitation. In all experiments aimed at the verification of the law of universal gravitation, macroscopic test and probe masses have been used up to now. At present, experiments intended to verify the law of universal gravitation with the help of atomic interferometry are being lively discussed, which opens the door to the use of microscopic probe masses to verify the law of universal gravitation in the microworld.

One of the most accurate measurements performed with atomic interferometry was the measurement of the ratio $\hbar/m$ of two physical constants, Planck's constant and mass. The significance of this measurement stems from the fact that the mass enters quantum mechanical equations precisely in the form of this ratio. Until recently, the most exact value of $\hbar/m$ resulted from neutron diffraction by crystalline silicon. The precision of diffraction measurements is 8×10^{-7}. Experiments with the use of atom interferometers [26] yielded an accuracy of 14×10^{-9}, whence follows an accuracy of 7×10^{-9} for the fine structure constant.

The efforts of numerous research laboratories have led to the development of a variety of high-precision instruments based on an atom interferometer, which are intended for acceleration (accelerometer), gravitational field (gravitometers and gradiometers), and rotation (gyroscopes) measurements.

3.3 Atomic clock

A fundamental limitation on the accuracy of measurement of frequency and time in atomic clocks is the *measurement time* of the frequency of the atomic transition. In the primary cesium frequency standard, it is defined by the time of atomic transit through the probing field. The methods of laser cooling and atom optics have made a new type of atomic clock possible, called the *atomic fountain*. In this case, the duration of the measurement is larger by two orders of magnitude in comparison with that in the frequency standard involving a thermal atomic beam. In an atomic fountain, atoms are first cooled by laser radiation and are next captured by an atomic magnetooptical trap, in which they experience further cooling. The resultant cloud of ultracold atoms serves as the source of slow atoms in the fountain: with the help of a laser pulse, the cloud of cold atoms is thrown vertically up and the atoms, describing ballistic trajectories, cross the probing field in their upward motion. Owing to free-fall acceleration, the atomic velocity gradually subsides to zero and the atoms fall again, passing through the probing field for the second time. Therefore, the atoms experience a double passage through the probing field, in which the readout of atomic transition oscillations takes place. The long interaction time allows realizing a relative accuracy of 4×10^{-14} with atomic fountains.

3.4 Atomic nanolithography

Nanolithography is used to fabricate material structures ranging in size from a single atom to about 100 nm. These structures are of interest for both basic science and applications. The incentive to develop nanolithography is the 'race' for a high transistor density in a chip, described by Moor's law. According to this empirical law, in new microchip models, which make their appearance 1.5–2 years after the previous ones, the density of elements doubles. To date, lithography techniques involving ultraviolet radiation, electron and ion beams, X-ray radiation, scanning probes, and self-organization have been well developed. Each of these techniques has advantages and disadvantages: optical lithography is diffraction-limited; charged particle beam lithography encounters problems associated with mass production of structures and the significance of Coulomb repulsion; scanning probes, which manipulate single atoms, exhibit poor efficiency; self-organization fabrication still calls for a better understanding of physical processes. Meanwhile, an extensive quest is underway for alternative ways of making nanostructures, and the nanolithography based on atom optics holds much promise as a fabrication technique.

The title 'atomic nanolithography' is used in reference to a family of techniques for the making of nanostructures in which laser light is used as atomic microlenses. Diversified configurations of laser fields have been proposed for the atomic microlenses: traveling [32] and standing [33] waves, as well as spatially localized laser fields [34]. The most significant results have been obtained with microlenses produced by standing laser waves quasiresonant with atomic transitions. An atom in the nonuniform laser field of a standing wave experiences a dipole force. The beam of atoms passes through the standing wave whose frequency is shifted to the blue side of the spectrum relative to the atomic resonance, and is drawn in the nodes of the standing wave under the action of the dipole force (Fig. 4). One period of the standing wave is an atomic lens and has the spatial size $\lambda/2$.

The size of the focused atomic spot and hence the size of the nanostructure on the surface depend on several physical factors. The atomic beam has a finite divergence and, as a consequence, a spherical aberration of the atomic lens emerges. Its effect is suppressed by using laser cooling. The small transverse size of the atomic lens also brings diffraction

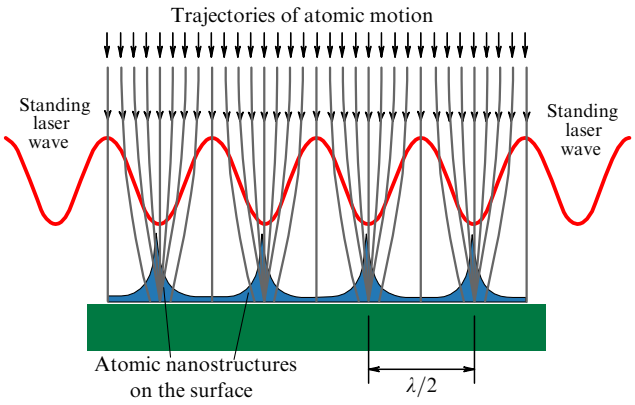

Figure 4. Atomic lens formed by a standing light wave.

aberrations into effect. For the atomic velocity about 200 m s^{-1}, the de Broglie wavelength is equal to about 0.01 nm; this wavelength corresponds to the diffraction limit $\sim \lambda/40$. The atoms experience the transverse velocity and spatial broadening owing to the spontaneous reradiation of laser photons. The broadening of atomic nanostructures is due to chromatic aberration and physical and chemical processes on the surface.

A standing light wave is ideally suited to the fabrication of one- and two-dimensional periodic structures — line and point arrays. The use of two orthogonally related interfering standing laser waves allows the formation of a two-dimensional array of 'photon microlenses' and the fabrication of two-dimensional nanostructures on a surface. By varying the wavelength, it is possible to change the grating period $\lambda/2$. By changing the polarization in the standing wave, it is possible to obtain the period equal to $\lambda/8$. Using the interference of three laser beams intersecting at 120° or five laser beams intersecting at 72° allows producing more complex quasiperiodic structures. To date, experiments on the focusing of atoms have been carried out on Na, Rb, Cs, Cr, Fe, Ni, Co, and Yb atoms. The prospect of experiments on aluminum, gallium, and indium atoms, which are of microelectronic interest, has also been considered. Figure 5 shows chromium nanostructures in the form of lines and spots [33]. The nanoline width at half maximum is 50 nm and the height is 28 nm. The smallest size of the nanostructures produced using the atomic microlenses of a standing wave is about 15 nm.

It follows from general physical considerations that in the construction of atom optics elements, an atomic lens in particular, preference should be given to spatially localized atom–field interaction potentials. Two types of localized fields are used for this purpose: the light field resulting from light diffraction by structures smaller than the light wavelength (Bethe holes) [34] and the light field localized in partially open waveguides. The diameter of a Bethe hole is smaller than the incident radiation wavelength. The field diffracted by the hole consists of a traveling wave field and a near-field component. The near-field component is used for making an atomic lens. The size of the minimal atomic spot in the focus of this lens, which may be equal to 0.1 of the optical wavelength, is determined by spherical and chromatic aberrations, atomic diffraction, interatomic interaction, and spontaneous radiation.

Another example of a localized laser field used for making an atomic lens is the field in a two-dimensional waveguide in which the interplane distance is of the order of or shorter than the wavelength of light; in the waveguide surfaces, there are two small coaxial holes whose radius is much smaller than the wavelength of light [34]. The radiation is barely transmitted through these small holes, but in the vicinity of each of them, the field is strongly modified inside and outside the waveguide. The character of modification depends on the polarization of the input radiation. The field distribution with an intensity minimum between the holes is referred to as a 'photon hole' and the distribution with an intensity maximum is termed a 'photon dot.' The photon dot and the photon hole can be used for focusing atomic beams.

Despite the numerous proposals concerning the focusing of atomic beams and the equally numerous experimental realizations of atomic lenses, this problem remains unsolved as regards construction of the images of nanoobjects of an arbitrary shape. The main complication is in the formation of the atom–electromagnetic field interaction potential that would approximate a 'perfect lens' for the atoms.

First implemented at the Institute of Spectroscopy, RAS, was an approach to nanostructure fabrication by the

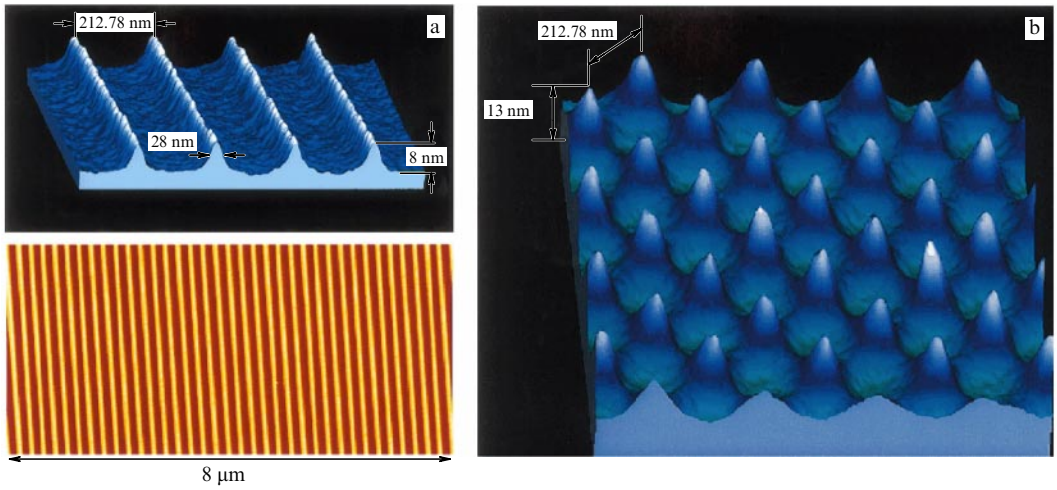

Figure 5. Chromium nanostructure images produced by focusing with (a) one-dimensional and (b) two-dimensional photon lens systems. The period of chromium lines and spots is $\lambda/2 = 213$ nm [33].

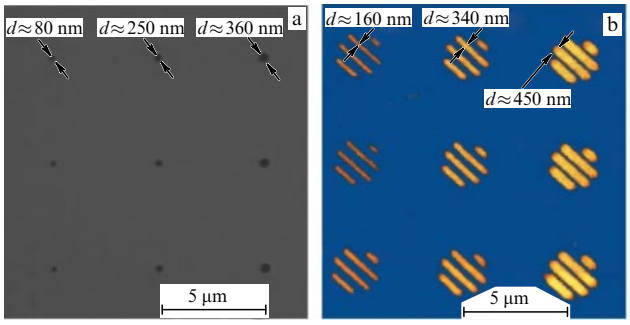

Figure 6. Production of nanostructures with the aid of an atom pinhole camera. The picture demonstrates the effect of nanohole diameter on the resolution of the atom pinhole camera. (a) Electron image of the membrane with nanoholes (atomic nanolenses) of various diameters: $d = 80$, 250, and 360 nm. (b) Images of nanostructures made of In atoms on the surface of silicon with the use of the nanoholes of the membrane shown in Fig. 6a [35, 36].

methods of atom optics, which is based on the analogy with a pinhole camera known in light optics [35, 36]. The atom pinhole camera comprises an atomic beam, a mask, a membrane with holes, and a substrate on which nanostructures are produced. The atoms transmitted through the mask, much as in optics, form a 'luminous object' with a geometry determined by the mask. The parameters of the atom pinhole camera are selected so as to maximize the resolution. The ratio between the mask–nanohole distance L and the nanohole–substrate distance l defines the 'demagnification' of the atom pinhole camera $N = L/l$. For $L = 10$ cm and $l = 10$ μm, the 'demagnification' is 10^4.

Masks in the atom pinhole camera are typically 10 μm in size, and the resultant nanostructures are therefore $N = 10^4$ times smaller, i.e., of the order of 10 nm. In this way, the objects of the *microworld* are transformed into *nanoworld* objects, and the atom pinhole camera can be considered a realization of Feynman's famous device: "...a scalable manufacturing system could be made which will manufacture a smaller scale replica of itself" [37].

In an atom pinhole camera, not only a single nanohole but also a nanohole array can be used (Fig. 6). Such a parallel pinhole camera has the capacity to simultaneously fabricate a large number of identical nanostructures of arbitrary atoms or molecules, with the minimal element size being equal to several nanometers. A simultaneous fabrication of 1 million identical nanostructures was demonstrated with an atom pinhole camera [35, 36].

4. Conclusions

Laser cooling as a method of achieving ultralow temperatures and atom optics as a new type of material particle optics have led to rapid progress in the area of modern physical technologies. Ultracold atomic ensembles, including quantum-degenerate Bose and Fermi gases, have become readily available to physical laboratories. Achievements in high-resolution optical spectroscopy have furnished tools for the coherent control over external and internal degrees of freedom of atomic matter. Atom optics, whose development has covered a relatively short period, has found practical uses in many areas, including atomic interferometry, quantum frequency and time standards, and atomic nanolithography. During the 20-year period of their development, atom interferometers have traveled the way from mere demonstration of their feasibility to the verification of basic physical laws and the making of the most precise quantum clock, accelerometers, gravitometers, and gradiometers. It is not unlikely that atom interferometers will find use in the detection of gravitation waves on Earth and in space. Another avenue of development showing great promise is an atom chip — an atom microtrap based on magnetic and light fields. This integrated micromanipulator of atomic waves is a candidate for quantum information technology. At present, atomic nanolithography is considered an alternative technique for nanolithography of the future. Further research in the areas of ultracold atoms and atom optics will allow a deeper understanding of quantum physics and will broaden the field of ultracold substance application in different technologies.

References

1. Hänsch T W, Schawlow A L *Opt. Commun.* **13** 68 (1975)
2. Andreev S V, Balykin V I, Letokhov V S, Minogin V G *Pis'ma Zh. Eksp. Teor. Fiz.* **34** 463 (1981) [*JETP Lett.* **34** 442 (1981)]
3. Letokhov V S, Minogin V G *Phys. Rep.* **73** 1 (1981)
4. Balykin V I, Minogin V G, Letokhov V S *Rep. Prog. Phys.* **63** 1429 (2000)
5. Lett P D et al. *J. Opt. Soc. Am. B* **6** 2084 (1989)
6. Kasevich M, Chu S *Phys. Rev. Lett.* **69** 1741 (1992)
7. Aspect A et al. *Phys. Rev. Lett.* **61** 826 (1988)
8. Migdall A L et al. *Phys. Rev. Lett.* **54** 2596 (1985)
9. Grimm R, Weidemüller M, Ovchinnikov Yu B *Adv. At. Mol. Opt. Phys.* **42** 95 (2000)
10. Raab E L et al. *Phys. Rev. Lett.* **59** 2631 (1987)
11. Balykin V I, Letokhov V S *Appl. Phys. B* **48** 517 (1989)
12. Aminoff C G et al. *Phys. Rev. Lett.* **71** 3083 (1993)
13. Ketterle W, Van Druten N J *Adv. At. Mol. Opt. Phys.* **37** 181 (1996)
14. Cornell E A, Wieman C E *Rev. Mod. Phys.* **74** 875 (2002); *Usp. Fiz. Nauk* **173** 1320 (2003)
15. Ketterle W *Rev. Mod. Phys.* **74** 1131 (2002); *Usp. Fiz. Nauk* **173** 1339 (2003)
16. DeMarco B, Jin D S *Science* **285** 1703 (1999)
17. Bloch I, Dalibard J, Zwerger W *Rev. Mod. Phys.* **80** 885 (2008)
18. Balykin V I, Letokhov V S *Phys. Today* **42** (4) 23 (1989)
19. Balykin V I, Letokhov V S *Usp. Fiz. Nauk* **160** (1) 141 (1990) [*Sov. Phys. Usp.* **33** 79 (1990)]
20. Balykin V I, Letokhov V S *Atom Optics with Laser Light* (Chur, Switzerland: Harwood Acad. Publ., 1995)
21. Meystre P *Atom Optics* (New York: AIP Press/Springer, 2001)
22. Balykin V I *Usp. Fiz. Nauk* **179** 297 (2009) [*Phys. Usp.* **52** 275 (2009)]
23. Mewes M-O et al. *Phys. Rev. Lett.* **78** 582 (1997)
24. Bloch I, Hänsch T W, Esslinger T *Phys. Rev. Lett.* **82** 3008 (1999)
25. Baudon J, Mathevet R, Robert J *J. Phys. B At. Mol. Opt. Phys.* **32** R173 (1999)
26. Cronin A D, Schmiedmayer J, Pritchard D E *Rev. Mod. Phys.* **81** 1051 (2009)
27. Balykin V I et al. *Phys. Rev. Lett.* **60** 2137 (1988)
28. Zurek W H *Rev. Mod. Phys.* **75** 715 (2003)
29. Blatt R, Wineland D *Nature* **453** 1008 (2008)
30. Jost J D et al. *Nature* **459** 683 (2009)
31. Balykin V I, Letokhov V S *Zh. Eksp. Teor. Fiz.* **94** 140 (1988) [*Sov. Phys. JETP* **67** 78 (1988)]
32. Balykin V I, Letokhov V S *Opt. Commun.* **64** 151 (1987)
33. McClelland J J "Nanofabrication via atom optics", in *Handbook of Nanostructured Materials and Nanotechnology* Vol. 1 (Ed. H Nalwa) (San Diego: Academic Press, 1999) p. 335
34. Balykin V, Klimov V, Letokhov V *Opt. Photon. News* **16** (3) 44 (2005)
35. Balykin V I et al. *Pis'ma Zh. Eksp. Teor. Fiz.* **84** 544 (2006) [*JETP Lett.* **84** 466 (2006)]
36. Melentiev P N et al. *Metamaterials* **3** 157 (2009)
37. Feynman R *J. Microelectromech. Syst.* **2** 4 (1993)

PACS numbers: **42.62.–b**, **42.82.–m**, **85.40.–e**
DOI: 10.3367/UFNe.0181.201108h.0884

New-generation vertically emitting lasers as a key factor in the computer communication era

N N Ledentsov, J A Lott

1. Introduction

At present, supercomputers are becoming one of the basic driving forces in the development of our civilization, providing progress in genomics, biomedical sciences, aerodynamics, mechanical engineering, predictions of natural cataclysms and technogenic impacts on the environment, and many other strategic fields of science and technology. Supercomputers play an important role in neural simulations and studies in the field of artificial intelligence. The development of high-speed telecommunications and internet technologies allows broad commercialization of high-performance computers and considerable broadening of the scope of their applications.

The continual decrease in the characteristic size of elements of the silicon integrated circuit leads to the doubling of the density of discrete elements on a crystal every two years. Correspondingly, processor efficiency and memory capacity drastically increase. To provide efficient data exchange among processors and the processors and memory or peripheral devices, it is necessary to increase the data transmission rate per channel. Communications among the elements of a system are gradually becoming its bottleneck, especially because of the necessity of constant scaling [1] of the spatial density of elements and the data transfer rate in the contacts of an individual integrated circuit (IC) and in all modules and boards. To support the scaling of the data transfer rate by preserving or reducing the size of interconnects, the data transfer rate per channel in all modern standards of electric interconnects should be approximately doubled every two to three years. For bit rates above 10 Gbit s^{-1}, the use of copper interconnects becomes complicated, and therefore the role of optical communication lines drastically increases. The modern supercomputer Blue Waters (IBM 2011) with a 10-petaflops efficiency (10^{16} flops: flops is the number of floating-point operations per second) already contains about five million optical interconnects, each of them operating at a bit rate of 10 Gbit s^{-1}. The tenfold increase in the supercomputer efficiency compared to the Roadrunner model (IBM, 5 Gbit s^{-1}) produced in 2008 resulted in an increase in the number of optical interconnects by two orders of magnitude. Supercomputers with the efficiency 20–30 times higher than that of the Blue Waters computer, which are expected in 2015, will use about a billion optical interconnects. In exaflop systems (10^{18} flops), up to 80% of the consumed power and up to 90% of the system efficiency will be determined by optical interconnects [1]. We note, however, that the manufacturing of energy-efficient, compact, and economical optical communication lines is far from a trivial problem for bit rates 50–100 Gbit s^{-1} per channel, which should be achieved in the near 3–6 years. In this brief review, we consider vertical-cavity surface-emitting lasers as the main element of modern short-range optical communication lines and discuss the outlook for a further increase in their bit rate in accordance with the requirements of computational systems in the nearest future.

[1] The term 'scaling' refers to a proportional change in physical sizes of components on a crystal. In silicon technology, the size of elements is constantly reduced with the basic geometry being preserved. This is called silicon scaling.

N N Ledentsov Ioffe Physical–Technical Institute, Russian Academy of Sciences, St. Petersburg, Russian Federation;
St. Petersburg Academic University, Scientific and Education Center of Nanotechnologies, Russian Academy of Sciences, St. Petersburg, Russian Federation
VI Systems GmbH, Hardenbergstr. 7, 10623 Berlin, Germany
E-mail: nikolay.ledentsov@v-i-systems.com
J A Lott VI Systems GmbH, Berlin, Germany

Uspekhi Fizicheskikh Nauk **181** (8) 884–890 (2011)
DOI: 10.3367/UFNr.0181.201108h.0884
Translated by M Sapozhnikov; edited by A M Semikhatov

2. Basic applications and standards

The development of modern data processing systems is based on silicon microelectronics. The 1.4-fold scaling of the characteristic size of the IC every two years leads to an exponential increase in the computational efficiency of processors. The increase in the efficiency is mainly achieved by increasing the number of kernels on one IC (modern Intel processors contain 80 kernels). The characteristic topological size of an element has been reduced to 22 nm, while the required bit rates of input–output devices per channel equal to 26 Gbit s^{-1} (2.6×10^{10} bit s^{-1}) approximately correspond to the number of grains of sand it would take to form a line the length of Earth's diameter. We note that IC prototypes with elements 18 mm and even 14 nm in size are already being manufactured and are in operation. The size and bit rate scaling in silicon technology will be continued, resulting in a radical increase in loading in local data communication networks.

An important strategic standard for receiving and transmitting data in highly efficient computational systems is the Infiniband standard. The bit rate per channel is doubled every 2.5 years on average. By 2014, the bit rate should exceed 50 Gbit s^{-1}, while by 2016–2017, it should achieve 100 Gbit s^{-1}.

The scaling of the other most important interfaces is occurring similarly. The most popular standard used in data storage networks is the Fibre Channel standard. Here, the standardized bit rate per channel reached 14 Gbit s^{-1} already in 2009, while by 2012, the standardization of interfaces to 28 Gbit s^{-1} is expected. The use of copper communication lines at such bit rates is limited to the cable length of about 1 m and 10 cm on a board. From the standpoint of energy consumption, interference produced during operation, and the size of cables and connectors, the use of copper is impractical even at considerably smaller distances. A new standard appears in the market the year following its adoption and begins to dominate after approximately 2–2.5 years. When the 28 Gbit s^{-1} standard is adopted, the 14 Gbit s^{-1} interface will dominate in the market.

An important feature of some interfaces, for example, the Ethernet standard that dominates data communication and processing networks, is the necessity of scaling not only the bit

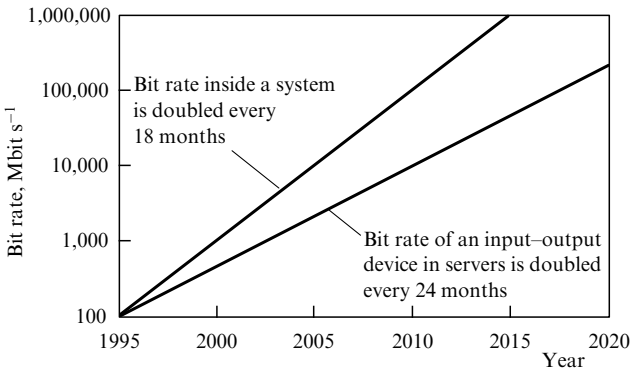

Figure 1. 'Road map' for the growth of the bit rate per channel in the Ethernet Standard (used in data processing centers) and the bit rate increase that is driven by advances in silicon integrated circuits. The number of transmission lines in the integrated system continuously increases (from 2 in 2000 to 10 in 2010), while the bit rate of an input–output device increased from 500 Mbit s^{-1} to 10 Gbit s^{-1} in the same period.

rate per channel but also the number of channels (Fig. 1). Thus, the spatial region allotted per channel on a commutation board having invariable size should decrease along with a simultaneous increase in the operational speed of the interconnect. The increase in the bit rate inevitably leads to an increase in the role of electromagnetic interference. Therefore, the trends of increasing the bit rate per channel and developing more and more compact receiver–transmitters obviously contradict each other.

In the area of interfaces in the consumer market, the Thunderbolt interface used in Apple devices (MacBook, iMac) has the highest bit rate per channel. It can be expected that electric interconnects in consumer electronics will be rapidly changed to optical interconnects (for example, using the Intel Lightpeak technology)

3. Modulated-current vertical-cavity surface-emitting lasers

At present, vertical-cavity surface-emitting lasers (VCSELs) dominate in optical data communication systems [2]. Unlike double-heterostructure stripe lasers [3], where light propagates parallel to the surface of epitaxial layers along a semiconductor waveguide with the refractive index higher than that of the layers surrounding the waveguide, the radiation of VCSELs is emitted perpendicular to the substrate surface. Individual devices of such a design and their arrays can be manufactured by using planar technology and can have a very small size in the plane of a wafer. As a result, the production of good structures has proven to be high, while the production cost of an emitter is low. In both cases, the active region is formed by the layers of a material with a smaller band gap, into which nonequilibrium charge carriers are injected. Currently, layers containing quantum wells, quantum wires, and quantum dots are used most extensively [4] because they considerably improve the properties of lasers. For example, InAs quantum dots allow the fabrication of VCSELs and stripe lasers emitting at 1.3 μm [5] by using the standard and economical arsenide–gallium technology. Stripe lasers have demonstrated the unique temperature stability of parameters, emission at temperatures above 220 °C, and bit rates upon direct current modulation higher than 25 Gbit s^{-1} per channel [6].

3.1 Laser geometry

An outline of a modulated-current VCSEL is shown in Fig. 2. The laser consists of a microresonator with a planar resonance cavity whose thickness is a multiple of half the wavelength. Inside the cavity is located the active medium into which nonequilibrium charge carriers are injected, in which population inversion is produced, and in which amplification occurs per transit of light in the vertical direction. Multilayer structures of alternating layers approximately a quarter of the wavelength in thickness of the higher and lower refractive indices (for example, made of $Al_xGa_{1-x}As$ with low and high aluminum content, respectively) are located above and below the microcavity. This sequence of layers satisfies the Bragg condition and provides the high reflectivity of mirrors, such that the light loss upon reflection from the mirrors remains lower than the gain per transit, and lasing is possible. The structure is grown on a GaAs substrate. The AlAs layers in the microcavity region are subjected to selective oxidation in water vapor to form a current aperture and restrict the optical modes of the microresonator by a region with a lower refractive index. An advantage of the gallium arsenide–aluminum arsenide system for VCSELs is the possibility of growing the layers of a Bragg reflector by using binary AlAs and GaAs compounds or quasibinary solid solutions with small amounts of gallium or aluminum. Because the heat conduction of binary solutions is an order of magnitude higher than that of the solid solution, the active medium is not overheated and the construction of the laser is simplified. In addition, because the jump of the refractive index in each aluminum arsenide–gallium arsenide interface exceeds 0.5, the total thickness of multilayer reflectors is small (about 3–3.5 μm per multilayer mirror), which also facilitates heat transfer and reduces the cost of the epitaxial growth. The large jump in the refractive index produces a broad ledge (60 nm) in the reflection spectrum of a multilayer mirror, simplifying requirements for the accuracy of the epitaxial growth control, thereby increasing the production of good wafers and reducing their cost.

The emission wavelength of the laser is determined by the photon resonance energy and, correspondingly, by the thickness of the microcavity layer, rather than by the band

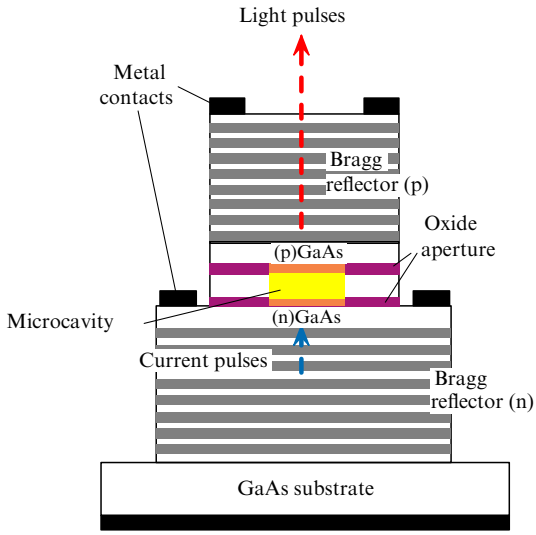

Figure 2. Schematic view of a modulated-current vertical-cavity surface-emitting laser.

gap of the active medium, as in a stripe laser. Because the band gap changes with temperature much faster than the photon resonance energy, the amplification spectrum of the active medium should be rather broad (no less than 50 nm) to provide lasing in the entire required temperature range. The optical design of VCSELs should provide:

(i) the optimization of parasitic radiation modes with the maximum enhancement of the interaction of the active medium with a vertical emission mode [7], for example, by using the antiwaveguide design of the VCSEL microcavity;

(ii) the optimization of oxide aperture layers to provide the specified mode composition of radiation in the transverse direction, for example, to obtain single-mode radiation;

(iii) the optimization of the transmission coefficient of the mirrors along with the optimization of the number of periods in the Bragg reflector or the use of several resonance cavities to provide the required photon lifetime in the microcavity.

3.2 Active medium

Figure 3a schematically shows a bulk semiconductor, a quantum well (QW), an array of quantum wires (QWs), and an array of quantum dots (QDs), and Fig. 3b schematically shows the density of states (dashed curves) and the occupation of states by charge carriers (solid curves) for active regions of different dimension.

The use of reduced-dimension heterostructures [8] in VCSELs plays a very important role for several reasons. First, the higher the differential gain of a laser is, the higher its operating speed for a similar geometry and the same operating current. The differential gain of QW lasers is mainly determined by the number of QWs and the dispersion of the subband of heavy holes, which can be controlled by stresses in the case of elastically stressed QWs. The differential gain of QD lasers is determined by the lateral density of QDs, which can be rather high for lasers emitting at 850 nm (more than 10^{12} cm^{-2} per QD layer), which allows obtaining the giant differential and modal gains.

Figure 4a shows a high-resolution transmission electron micrograph of InAs QDs produced by the molecular beam epitaxy (MBE) method in an $Al_xGa_{1-x}As$ matrix emitting at 850 nm [9]. Figure 4b presents photoluminescence spectra of

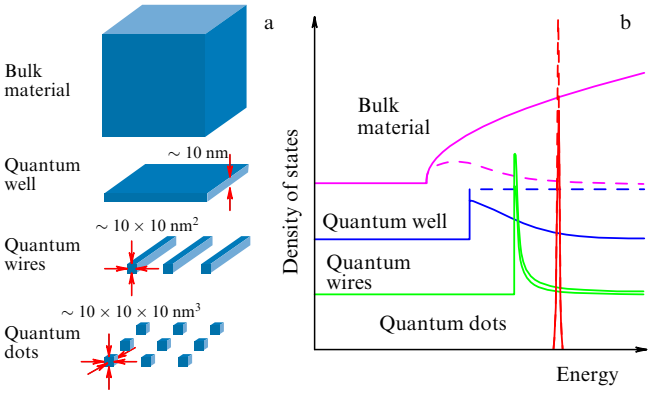

Figure 3. (a) Schematic view of a bulk semiconductor, a quantum well (QW), an array of quantum wires (QWs), and an array of quantum dots (QDs). (b) Schematic view of the density of states (dashed curves) and the occupation of the states by charge carriers (solid curves) for active regions of different dimensionalities. In real structures containing QDs and QWs, the spectrum of the density of states is broadened due to both the inhomogeneous broadening (caused by the dispersion of QWs and QWs over shape and size) and the homogeneous broadening caused, for example, by interaction with phonons.

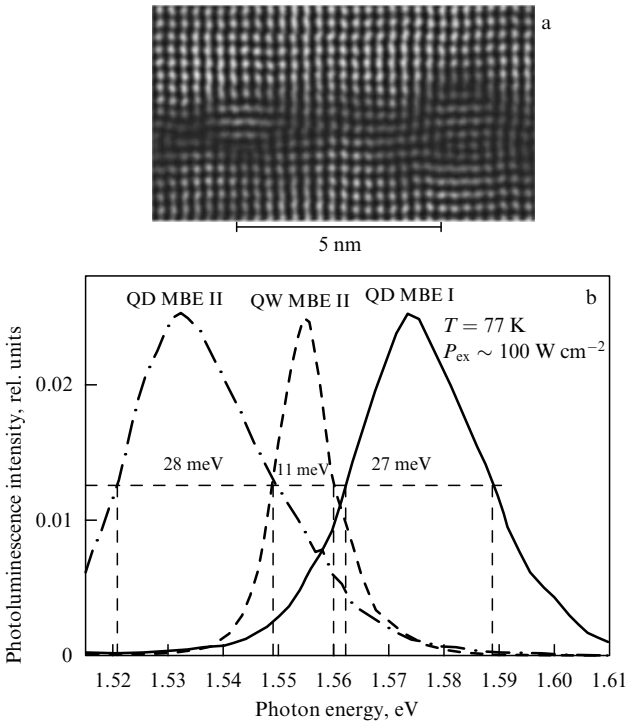

Figure 4. (a) Image of InAs QDs in an $Al_xGa_{1-x}As$ matrix emitting at 850 nm. The inverted-line-contrast regions contain InAs in amounts higher and lower than 20%. (b) Photoluminescence spectra of InAs QDs and GaAs QWs at 77 K.

InAs QD structures and GaAs QW structures at low temperature (77 K). It can be seen that luminescence spectra of QD structures at moderate pump powers are considerably broader than those of QW structures. But the situation drastically changes at high current densities, and the amplification spectra of QDs are typically considerably narrower than the structureless broad amplification spectra of QWs caused by the step density of states (see Fig. 3).

3.3 Operation speed of VCSELs

In the case of stimulated emission, the radiative recombination time is inversely proportional to the optical field intensity in a resonator; for VCSELs, this means the necessity of increasing the current density for reducing the time of stimulated emission upon annihilation of the injected electrons and holes. At the same time, the decrease in the radiative recombination time leads to a sublinear dependence of the density of nonequilibrium carriers and the field intensity on the current density. The resonance frequency that characterizes the system response to a step change in the current and hence the operation speed of the laser also strongly depends on the current density. Because the period of resonance oscillations consists of positive and negative half-waves, the signal rise and decay time are approximately equal to the quarter of the period. The maximum rate of optical pulse transfer without distortions in the absence of a considerable damping is determined by the sum of the signal rise and decay times and is therefore approximately equal to the doubled resonance frequency. To double the resonance frequency and operation speed, the pump current density should be increased fourfold. However, the doubling of the pump current of a VCSEL drastically reduces its service life (by 30–40 times). This is related to the overheating of the active region and a high probability of nonradiative recombination

(for example, Auger recombination) accompanied by energy transfer to a crystalline lattice, including the generation of defects. Because 10 Gbit s^{-1} GaAs QW VCSELs already operate near the current density at which the overheating of the laser begins and its output power and operation speed decrease, the achievement of resonance frequencies considerably exceeding 10 Gbit s^{-1} was considered unlikely. The use of QDs as the active medium can considerably reduce the generation and growth rates of defects by restricting the diffusion transport of nonequilibrium carriers to regions with the enhanced rate of nonradiative recombination.

As mentioned above, controlling stresses in the active medium and (or) changing its dimension allow drastically increasing the differential amplification of the laser and achieving the same resonance frequencies at much lower current densities. The reduction in the oxide aperture thickness of the laser can also improve the frequency characteristics due to the improvement in heat transfer at the same current density and a decrease in the optical mode volume followed by the suppression of parasitic radiation. When photonic crystals or microcavities are used that provide the concentration of the optical field in one small-volume vertical mode, a very high operation speed can be achieved by using the Purcell effect even without the population inversion [10].

Figure 5 shows the dependence of the relaxation resonance frequency on the current in a cw VCSEL [11, 12]. It follows that in the case of small apertures, resonance frequencies of the order of 30 GHz are achieved. Correspondingly, by suppressing the parasitic decay in such VCSELs (caused, for example, by the high resistance and capacitance of the laser or by the long photon lifetime in the microcavity [13]), bit rates up to 50 Gbit s^{-1} and higher can be achieved. The maximum heat-removal operation temperature of such 850 nm VCSELs at which lasing is still observed reaches 200 °C, while the operation parameters of the laser at 100 °C change within 10–20%.

The presence of the high relaxation resonance frequency for using VCSELs in receiver–transmitter systems is not a sufficient condition. The laser should not emit intensity overbursts on applying rectangular current pulses, and arbitrary trains of unit current pulses should produce an optical signal of the same amplitude. The power accumulation effect in the laser cavity or, on the contrary, the photon depletion effect in the cavity, depending on the duration of pulses or intervals between them, leads to the 'floating' of the 'zero' (minimal signal) and 'one' (maximal signal) levels. Figures 6a and 6b show experimental 'eye diagrams' at 20 and 40 Gbit s^{-1}, obtained by using control integrated circuits and microassemblies of VCSEL transmitters and PIN photodetectors (produced by VI-Systems GmbH). We see that the one and zero levels are well discriminated over the signal level for any arbitrary train of pulses (when using the 2^7–1 PRBS measurement standard). For 40 Gbit s^{-1}, the error-free transmission (less than one error in 10^{12} pulses) was realized for a 1 mW optical power in a fiber (0 dBm). In the future, a drastic reduction in the optical power is expected for achieving the same noise level and increasing the operation speed. Figure 6c shows a microassembly containing a VCSEL and a control integrated circuit, and Fig. 6d shows a complete module connected with a multimode fiber (50 μm) used in the eye diagram measurements.

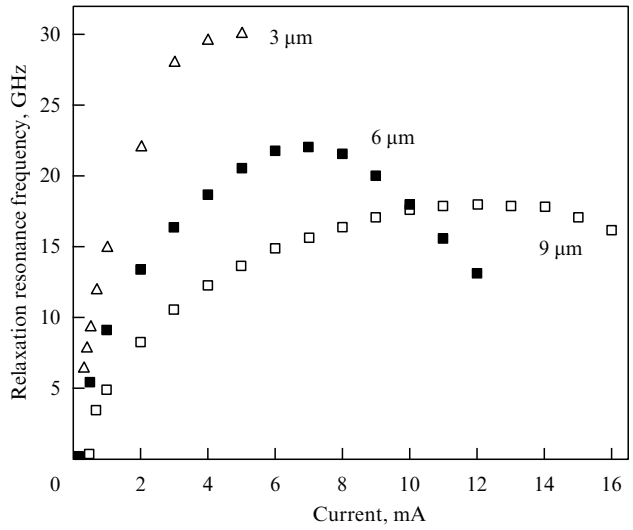

Figure 5. Dependence of the relaxation resonance frequency of a VCSEL on the pump current in the cw regime for different diameters of the oxide aperture of the laser.

3.4 Vertical-cavity surface-emitting lasers based on other $A^{III}B^{V}$ compounds

Vertical-cavity surface-emitting AlGaAs lasers emitting at 850 nm are in demand the most. First, all the most important short-range receiver–transmission standards use this wavelength. Multimode optical fibers, which also should be specially standardized, are adapted to this wavelength. The manufacturing of VCSELs based on InP, GaN, GaSb, and related solid solutions is a considerably more complicated problem, and their market is much smaller than that of GaAs VCSELs used to replace copper interconnects. The annual turnover of copper interconnects, not taking control circuits into account, was more than $130 billion in 2010. Vertical-cavity surface-emitting lasers emitting at 1.3 μm have a considerable market potential. These lasers can be used for transmitting signals over single-mode optical fibers and manufactured on GaAs [5] and InP [14] substrates. Work in this area actively continues. 1.3 μm VCSELs on GaAs substrates can be very easily manufactured by using QD technology. However, only a few groups exist in the world that possess the technological knowledge and equipment for growing QD lasers. To manufacture a QD VCSEL, it is also necessary to know the specific design of the laser for a given wavelength. The main problem in the manufacturing of lasers based on InP is the low heat conduction of solid (In, Ga, Al)As solutions and the low contrast of the refractive index of multilayer Bragg mirrors. The thickness of a multilayer mirror required to obtain the same reflectance as that of GaAs – AlAs mirrors is twice as large and the heat conduction 30 times lower than for GaAs – AlAs mirrors. The width of the reflection ledge is small (25 nm) and requires the high-precision control of epitaxial growing, while the use of InP substrates and a long growing time lead to a high cost of epitaxial VCSEL structures. In addition, because the selective oxidation technology cannot be used for these materials, the injection region is formed by the method of a local tunneling junction with selective etching, followed by epitaxial growth, which additionally complicates the technology.

3.5 Alternative approaches in VCSEL construction

To overcome the problems considered above, we proposed a solution based on the use of passive resonators. It is known

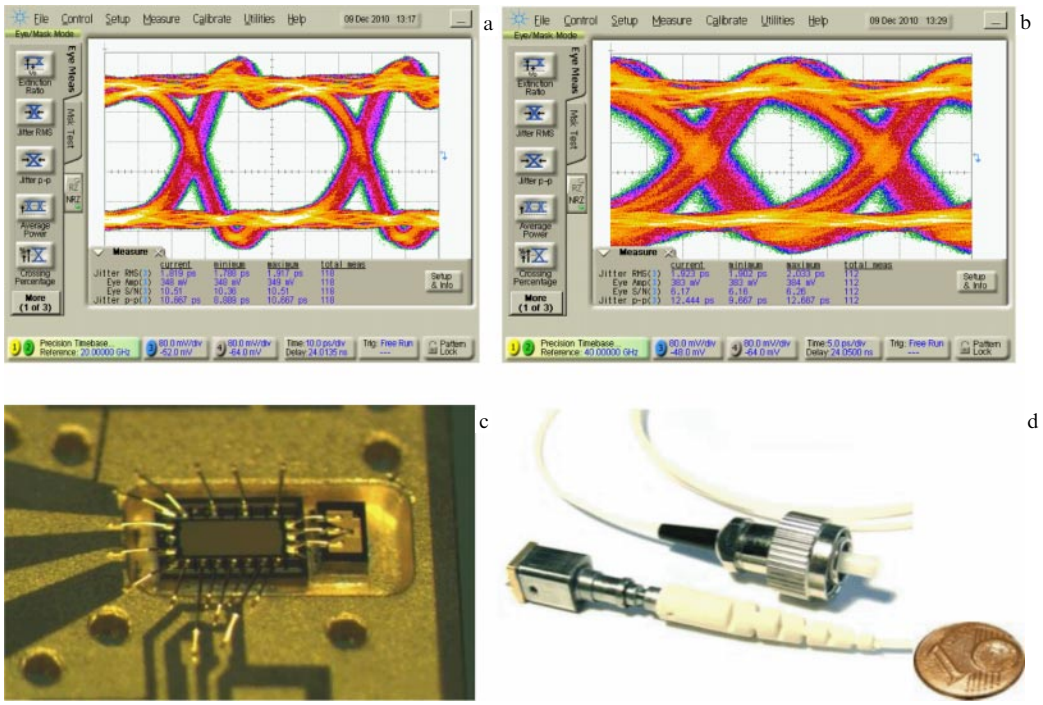

Figure 6. Experimental 'eye diagrams' obtained for bit rates (a) 20 Gbit s^{-1} and (b) 40 Gbit s^{-1} by using microassemblies of VCSEL transmitters and PIN photodetectors (VI-Systems GmbH). (c) Microassembly of a VCSEL and control integrated circuit. (d) Complete module connected with a multimode fiber (50 μm).

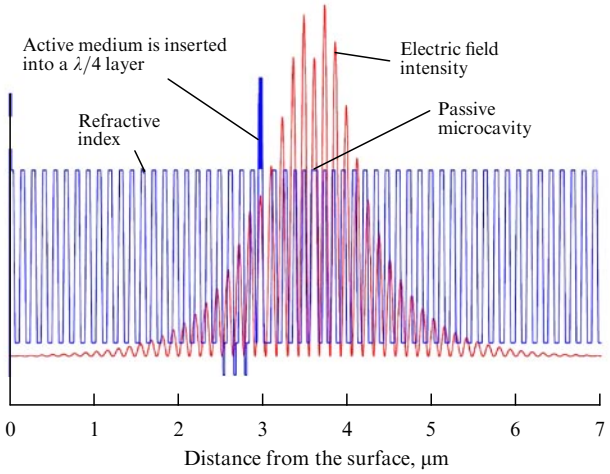

Figure 7. Design of a passive microcavity VCSEL.

that the high-Q resonator approximation can drastically change the radiation pattern and radiation lifetime of an oscillator. This led to the idea of manufacturing a VCSEL with a passive microcavity. In this case, the active medium is introduced into the Bragg reflector layer in the region of the noticeable decay of the optical field, while the microresonator remains 'empty' [15] (Fig. 7). Such a laser operates similarly to a usual VCSEL up to transition temperatures above 130 °C [15]. At first glance, such a design seems to have low efficiency because the field intensity in the active medium decreases compared to that in the passive microcavity. However, not the absolute intensity but the relative field intensity is in fact important. Therefore, for example, when a dielectric resonator is used with the giant power density of the optical mode caused by a giant jump of the refractive index (up to 2 and more) on the interfaces of dielectric Bragg reflectors, the field intensity in the active medium, even reduced several-fold, considerably exceeds the field intensity in the field maximum when Bragg mirrors are based on 'related' semiconductors with a small jump of the refractive index and, correspondingly, a broad field distribution. The dramatic reduction in the thickness of 'residual' semiconductor Bragg mirrors, if they are needed at all, provides an efficient heat conduction of the device.

The presence of a passive microcavity opens the possibility of producing photonic crystal structures in it, inserting metal nanostructures, using nanoimprint technology, applying materials with giant electrooptical or piezoelectric effects for controlling the emission wavelength, etc., without worrying about the current flow, nonradiative recombination, and heat conduction in the active medium.

4. Electrooptically modulated vertical-cavity surface-emitting lasers

Simultaneously with the development of the technology of directly modulated VCSELs, work on the development of electrooptically modulated VCSELs continues. In this case, as shown in Fig. 8, the alternating voltage is applied to the electrooptical modulator (EOM) section vertically integrated with the laser section operating in the cw regime. A change in the refractive index in the active medium of the EOM (for example, a superlattice) caused by the electric field leads to a spectral shift of the resonance in the transmission spectrum of the EOM section. Correspondingly, the light from the VCSEL section is either emitted from the laser or blocked [16]. Depending on the operation regime, the VCSEL section can operate at very low current densities, having an extremely long service life. On the other hand, the EOM

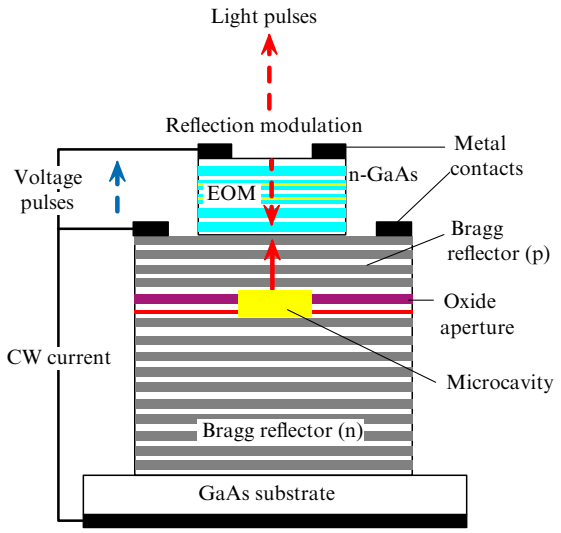

Figure 8. Electrooptically modulated VCSEL. A change in the transmission coefficient of the EOM section in the case of a reverse bias applied to the p–i–n junction in the EOM section having a low capacitance provides ultrahigh operational frequencies of the laser.

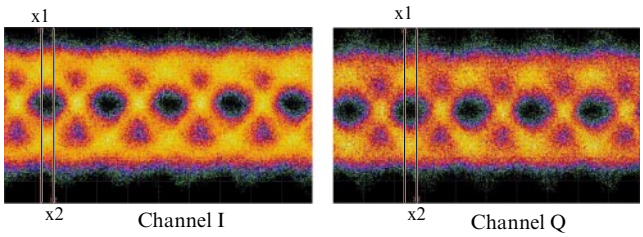

Figure 9. 'Eye diagrams' of an EOM VCSEL obtained in the QPSK multilevel coding mode for a bit rate of 10 Gbit s^{-1} per channel (the total bit rate in the line is 20 Gbit s^{-1}) at a carrier frequency of 13 GHz.

section operating in the reverse bias regime has an extremely low capacitance and can provide operation frequencies equal to 60 GHz [7] and above.

A distinct feature of EOM VCSELs is the high linearity of their characteristics [7], which allows realizing multilevel coding [17]. Figure 9 shows eye diagrams of an EOM VCSEL with the bit rate 10 Gbit s^{-1} per channel (the total bit rate is 20 Gbit s^{-1}) with the use of QPSK coding at the carrier frequency of 13 GHz.

Error-free data transfer was realized at the bit rates up to 16 Gbit s^{-1}. Rapid progress in this field of VCSEL applications can be expected in the near future.

5. Conclusions

Modern VCSELs represent a complex combination of micro- and nanotechnologies. The small size of and low power consumed by the laser in both the current and EOM versions give promise that energy-efficient optical interconnects with bit rates of 50–100 Gbit s^{-1} per channel will be realized and used in new-generation supercomputers, data storage and processing centers, and electronic devices in the consumer market.

The authors thank Zh I Alferov, D Bimberg, S A Blokhin, A E Zhukov, V M Ustinov, and V A Shchukin for the useful discussions. The work was supported by the European Union (grant FP7/2007-2013 according to the VISIT Project Agreement No. 224211) and the Eurostars EC program (the Optical Link Project).

References

1. Benner A "Optical interconnects for HPC", in *Short Distance High Density Optical Interconnects Workshop. An OIDA Roadmapping Workshop, Stanford, CA, April 12–13, 2011*
2. Iga K *IEEE J. Select. Topics Quantum Electron.* **6** 1201 (2000)
3. Alferov Zh I *Fiz. Tekh. Poluprovodn.* **32** 3 (1998) [*Semiconductors* **32** 1 (1998)]
4. Ledentsov N N, Bimberg D, Alferov Zh I *J. Lightwave Technol.* **26** 1540 (2008)
5. Lott J A et al. *Electron. Lett.* **36** 1384 (2000)
6. Tanaka Yu et al. "25 Gbps direct modulation in 1.3-μm InAs/GaAs high-density quantum dot lasers", in *Conf. on Lasers and Electro-Optics, OSA Technical Digest* (Washington, DC: Optical Society of America, 2010) CD, paper CTuZ1
7. Ledentsov N N, Hopfer F, Bimberg D *Proc. IEEE* **95** 1741 (2007)
8. Dingle R, Henry C H "Quantum effects in heterostructure lasers", U.S. Patent No. 3982207, September 21, 1976
9. Ledentsov N N et al. *Proc. SPIE* **7224** 72240P (2009)
10. Bennett A J et al. *Appl. Phys. Lett.* **90** 191911 (2007)
11. Mutig A et al. *Appl. Phys. Lett.* **95** 131101 (2009)
12. Ledentsov N N et al. *Proc. SPIE* **7952** 79520J (2011)
13. Westbergh P et al. *Electron. Lett.* **46** 938 (2010)
14. Hofmann W, Amann M-C *IET Optoelectron.* **2** 134 (2008)
15. Lott J A et al. *Electron. Lett.* **47** 717 (2011)
16. Shchukin V A et al. *Proc. SPIE* **6889** 68890H (2008)
17. Crisp M J et al. *Proc. SPIE* **7933** 79331D (2011)

PACS numbers: **42.65.–k**, **42.70.–a**, **78.67.–n**
DOI: 10.3367/UFNe.0181.201108i.0891

The photonics of self-organizing biomineral nanostructures

Yu N Kulchin

1. Introduction

The possibilities of using optical radiation for the transmission and processing of more and more increasing volumes of information are stimulating the search for principally new technologies aimed at developing the requisite components for communication systems and devices for generating and detecting radiation, and designing optoelectronic computers. Nanophotonic objects such as photonic crystals have been attracting increasing attention recently as promising systems for solving such problems [1]. It is known that Nature has already created various materials with photonic crystal properties, the diversity of these materials including noble opal, the pollen of the butterfly's wing, the beetle's chitin shell, and the mother-of pearl of a shell which grow due to self-organization — one of the most promising technologies. The basic structural components of living systems almost entirely consist of ordered arrays of protein and hydrocarbon molecules. This specific feature of living systems is due to the ability of biological macromolecules to self-organize in

Yu N Kulchin Institute of Automatics and Control Processes, Far-East Branch of the Russian Academy of Sciences, Vladivostok, Russian Federation. E-mail: kulchin@iacp.dvo.ru

Uspekhi Fizicheskikh Nauk **181** (8) 891 – 896 (2011)
DOI: 10.3367/UFNr.0181.201108i.0891
Translated by M Sapozhnikov; edited by A Radzig

solutions [2]. The latter property allows the manufacturing of uniquely intricate nanostructures, providing high efficiency per unit mass without putting in extreme requirements for primary materials and energy. Unfortunately, most natural protein complexes are unstable to temperature variations and chemical actions and can also be easily damaged by bacteria. As a result, direct analogues of biological systems have not found wide applications for manufacturing ordered nanostructures.

At the same time, a rather broad group of biological organisms exists which can concentrate in themselves mineral substances, which are contained in extracellular structures formed by complex composite substances — biominerals. Because they contain two components, organic (proteins or polysaccharides) and mineral (salts or oxides of elements), these self-organizing structures are stable against the action of many environmental factors [2].

A spectacular example of organisms with metabolism based on the self-organizing biomineralization is deep-sea glass sponges (DSGSs), which possess a cellular mechanism of selective accumulation of silicon from water and a complex protein-functioning mechanism, jointly providing the construction of a skeleton system from ordered silicon dioxide nanostructures [2, 3].

In this connection, the study of the morphology and physical and chemical properties of elements of the biomineral skeleton in these objects, in which a mineral component is represented by silicon dioxide, and of the biosilicification process itself in living nature, is of great interest for the development of nanotechnologies.

Along with investigations of biomineralization processes in living nature, researchers in many laboratories are attempting to synthesize biomineral materials with the help of available biopolymers: proteins and polysaccharides. In doing so, biomimetic nanostructured materials are synthesized by sol-gel chemistry methods, which are mainly used in the synthesis of inorganic oxides of silicon, titanium, aluminium, and other chemical elements and are complementary to chemical processes proceeding in living systems.

This paper presents the results of studies on the structure, chemical composition, optical, and nonlinear optical characteristics of DSGS spicules and their artificial biomimetic analogues as new materials for photonics.

2. Morphology and physicochemical characteristics of glass sea sponges

There are about 2000 species of sea sponges, of which about 500 belong to hexacorallia DSGSs [4]. In this paper, we introduce the results of studies of the three types of DSGSs: *Hyalonema sieboldi*, *Pheronema sponge*, and *Sericolophus hawaiicus*, which mainly inhabit the southern seas of the Pacific Ocean. A photograph of a typical sample of sponges of this type is displayed in Fig. 1a. Basal (anchor) spicules of these sponges, which can reach up to 1 m in length, possess an extraordinary elasticity, allowing one to literally knot them (Fig. 1b), whereas skeletal spicules are rather rigid. We selected for studies samples of basal spicules homogeneous over the thickness with lengths from 20 mm to 50 cm and diameters from 40 μm to 1 mm.

A detailed scanning electron microscopic (SEM) study of the transverse sections of basal spicules shows that each of them consists of many axial concentric layers, their number varying from a few dozen to a few hundred, depending on the sponge type and age (Fig. 1c). Each of the concentric layers of a spicule consists of silicon dioxide nanoparticles 20 to 120 nm in size closely packed in a matrix formed by collagen-like nanofibrils and separated between themselves by nanometer protein layers (Fig. 1c) [3, 5, 6]. All the spicules have a central nucleus representing an axial protein filament 1–2 μm in diameter, localized as shown in Fig. 1, and a set of surrounding silicon dioxide and protein component layers [7]. The thickness of layers containing silicon dioxide particles is more than 100 times larger than the thickness of separating protein layers.

Studies performed by the method of energy-dispersive X-ray spectrometry have given evidences that spicules consist mainly of silicon (max $\sim$ 33%), oxygen (max $\sim$ 66%), and carbon (max $\sim$ 9%), with trace amounts of Na and K [8, 9]. It was also established that the chemical composition of the layers is not constant and depends on their location, the sponge shape, and the spicule type.

The study of mechanical characteristics of basal spicules by the method of dynamic ultramicrohardnessmetry [7, 10] have shown that the Young modulus for basal spicules of sea sponges is close to its value for natural opal. It was found that the distribution of the Young modulus over the transverse section of a basal spicule is inhomogeneous and changes from its periphery to center from 33,000 to 40,000 GPa. The

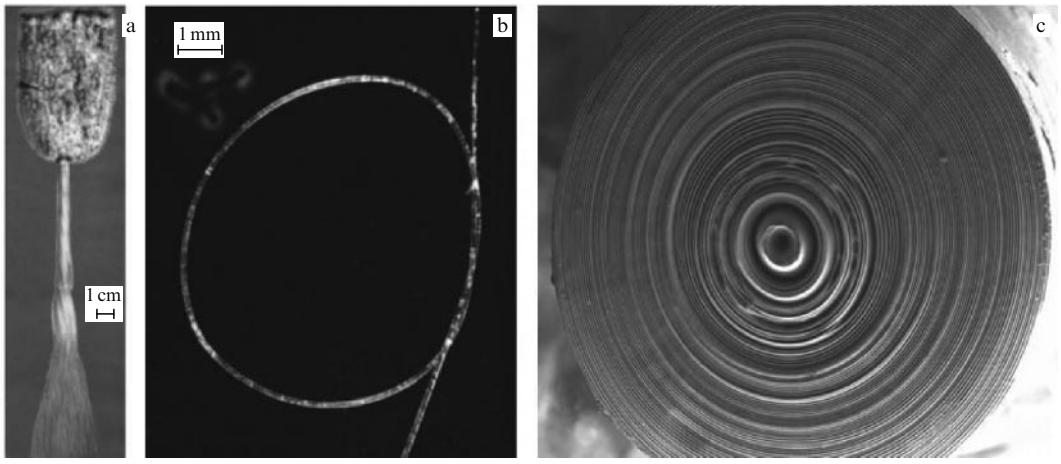

Figure 1. Photographs of *Hyalonema sieboldi* DSGS (a), a fragment of its basal spicule (b), and an SEM photograph of a processed end of a spicule (1157× magnification) (c).

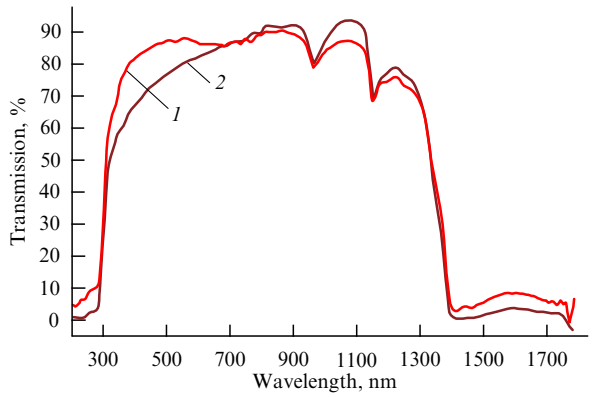

Figure 2. Transmission spectra of *Pheronema raphanus* DSGS spicule materials: curve *1*, basal spicule; curve *2*, skeletal spicule.

mechanical properties of basal spicules observed in experiments are determined by their layered structure and the presence of an organic matrix [3, 9], providing their enhanced mechanical strength and flexibility.

The distribution of the refractive index of a basal spicule over its section measured by the interferometric method [11] demonstrated that the refractive index of layers surrounding the central axial filament is about 1.45–1.48 and decreases to 1.39–1.41 at spicule edges [5, 7], in good agreement with the results reported in paper [11].

The transmission spectrum of the spicule material was recorded in the range from 200 to 1700 nm [9]. Figure 2 demonstrates the transmission spectrum of a *Pheronema raphanus* basal spicule, which is typical for spicules of all types studied here. One can see that the spicule material transmits radiation rather well in the visible and near-infrared spectral ranges. The absorption lines observed at 770, 960, and 1150 nm belong to hydrated silicates contained in spicules, which is consistent with the results obtained in Ref. [11] for basal spicules of a *Hyalonema sieboldi* sponge and other types of sea sponges [3]. The average power loss of the 633-nm laser radiation in the waveguide propagation mode was about 0.1 dB m^{-1} for almost all the spicules studied in our work. The experimental studies of the transverse intensity distribution of radiation propagating in spicules showed that the radiation was concentrated in the axial region ~ 20 μm in size and its spatial distribution was nearly Gaussian [12, 13].

The layered structure of basal spicules also gives rise to the periodic variation of the refractive index over the transverse section on the nano- and micrometer scales. In such a layered structure, the guided radiation modes can propagate with an effective refractive index lower than the refractive index of silicon dioxide. These modes are strongly coupled with light-guiding axial layers. Because of the great difference between the refractive indices of alternating axial layers, the radiation power flux is strongly reflected in the radial direction. In this case, due to a great number of layers in a spicule, for certain values of the effective refractive index of propagating modes the phasing condition can be fulfilled for light fluxes propagating in layers, thereby reducing radiation losses [14].

As shown in papers [12, 15], light can propagate in DSGS spicules only at certain angles to the spicule axis. The resonance wavelength of such a radiation will directly depend on the thickness of layers with a high refractive index. As a result, basal spicules should have forbidden bands, similar to those in photonic crystals. Because the thickness of axial layers with a high refractive index is small, resonance conditions will be fulfilled for the waves propagating at angles close to $\pi/2$ with respect to the normal to the spicule axis. This means that the single-mode propagation regime with the increased size of the mode spot is preferable for radiation guided in basal DSGS spicules. The results of numerical simulations show that this size can reach $\sim 20\,\lambda$ [12]. As the layer thickness is varied from 200 nm to 1 μm, the wavelength resonances of guided radiation will lie in the spectral range from 300 to 1200 nm, in good agreement with experimental findings.

To confirm the presence of photonic crystal properties of basal spicules in glass sea sponges, the propagation of extremely low-energy ≈ 0.01-nJ pulses through them was additionally investigated. Forty-fs, 800-nm pulses were generated by a Ti:sapphire laser at a repetition rate of 1 kHz. The emission spectrum of the laser is presented in Fig. 3a. As expected, the spectra of transmitted radiation for all basal spicules exhibited oscillations. This is illustrated in Fig. 3b by the transmission spectrum of a basal spicule 190 μm in diameter and 40 mm in length, with the central channel ≈ 2 μm in diameter and ≈ 280-nm-thick axial layers with a high refractive index. Experimental studies have given evidences that due to biological growth the thickness of axial layers of basal spicules deviates somewhat from measured average values. Because of this, according to Ref. [14], the maxima of the experimental transmission

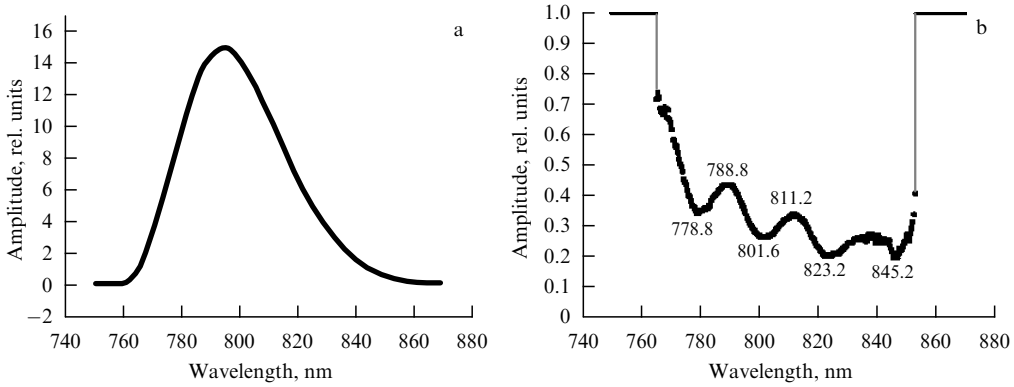

Figure 3. Radiation spectra of ultrashort pulses before (a) and after (b) transmission through a *Hyalonema sieboldi* DSGS spicule (40 mm in length and 190 μm in diameter).

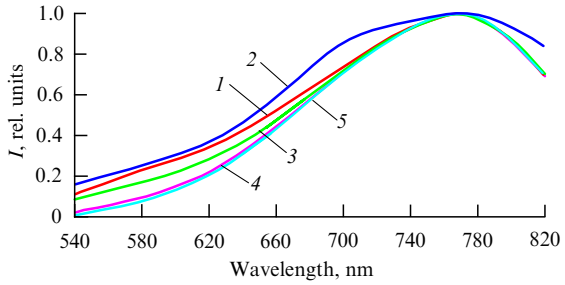

Figure 4. Normalized fluorescence spectra of a *Hyalonema sieboldi* basal spicule at different relative excitation energies of 532-nm, 12-ns input pulses (pulse repetition rate is 10 Hz, the maximum pulse energy is 30 mJ). Attenuation coefficients of the pulse energy are 1 (curve *1*), 0.3 (*2*), 0.2 (*3*), 0.13 (*4*), and 0.1 (*5*).

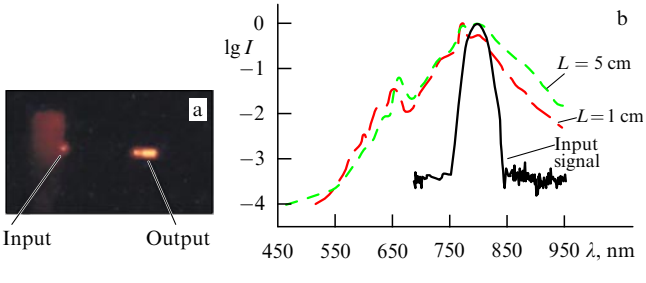

Figure 5. (a) Photograph of supercontinuum generation by 40-fs, 800-nm, 100-nJ ultrashort pulses in a *Hyalonema sieboldi* sponge spicule 200 μm in diameter and 1.5 cm in length. (b) Supercontinuum spectrum after the transmission of pulses through a *Sericolophus hawaiicus* sponge spicule 250 μm in diameter.

spectrum are found to be somewhat smoothed and superimposed on a pedestal, resulting in the comparatively smooth spectrum as a whole.

Thus, the studies have shown that the presence of periodic axial cylindrical silicon dioxide layers in basal DSGS spicules leads to the formation of forbidden photonic bands in them and, therefore, spicules of deep-see glass sponges represent a new type of natural photonic crystals.

3. Nonlinear optical properties of DSGS spicules

Upon excitation of basal spicules by 12-ns, 30-mJ, 532-nm second harmonic pulses from an Nd:YAG laser at a pulse repetition rate of 10 Hz, a considerable increase in the fluorescence intensity in the long-wavelength region was observed [7]. Figure 4 demonstrates the normalized fluorescence spectra of basal spicules 140 μm in diameter and 5 cm in length obtained at different pumping radiation intensities. One can see that the spectra have a maximum in the long-wavelength region at 770 nm, whose position is independent of the laser excitation intensity at the spicule entrance. The spectra differ greatly from the relevant fluorescence spectrum of a usual multimode silica fiber [13]. This is probably explained by the presence of large organic complexes in spicules of glass sea sponges. The measurements of the dependence of the maximum fluorescence intensity at 770 nm on the excitation power showed that this dependence saturated when the excitation power was increased more than 10-fold. This demonstrates the nonlinearity of the light-energy transformation in spicules related to a high concentration of organic complexes inhomogeneously distributed in them [16]. A specific feature of glass sea sponges is their fluorescence lifetime. The fluorescence lifetime of basal spicules measured at different excitation powers reaches a few dozen microseconds, considerably exceeding these lifetimes, for example, for sea zooplankton or quartz optical fibers ($\approx 10^{-10}-10^{-9}$ s) [17].

A unique property of glass sea spicules as optical fibers with a periodically changing transverse distribution of the refractive index is the complicated frequency profile of the dispersion for light pulses propagating in them, which substantially differs from analogous profile for conventional optical fibers. As a result, new nonlinear-optical phenomena and new regimes of spectral–temporal transformation of ultrashort light pulses can be observed in such 'optical fibers'.

In this connection, a model was constructed to describe the propagation of ultrashort pulses in spicules taking into account the combined action of dispersion effects, nonlinear polarization, and ionization nonlinearity leading to the self-phase modulation of the light field and efficient transformation of the pulse spectrum to a supercontinuum; in addition, the propagation of ultrashort pulses in DSGS spicules was numerically simulated and studied experimentally [18]. Experiments were performed using a Spitfire Pro Ti:sapphire laser complex (Spectra Physics, USA) emitting $\approx$ 0.9-mJ, 40-fs, $\approx$ 800-nm single pulses at a pulse repetition rate of 100 Hz with a spectral FWHM of 35 nm.

On coupling $\approx$ 5-nJ ultrashort pulses into different DSGS spicules 5–15 mm in length, the self-focusing of radiation was observed with the formation of 'hot regions' in the transverse intensity distribution of transmitted light beams. The shape of emission spectra in these regions noticeably changed [19]. The nonlinear-optical coefficient of the spicule material measured in the self-focusing of ultrashort pulses in spicules was $n_2 \approx 8.8 \times 10^{-16}$ cm^2 W^{-1}, which exceeds this coefficient for silica by more than three times, and by approximately 10^3 times for air.

As the laser pulse energy was increased above $\approx$ 20 nJ, the stable formation of a supercontinuum was observed in the spectrum of radiation transmitted through spicules, while prolonged repeated irradiation by 0.1–0.9-mJ pulses caused the optical breakdown of the spicule material. Figure 5a displays a photograph illustrating the transformation of the spectrum of a 100-nJ femtosecond pulse transmitted through a *Hyalonema sieboldi* sponge spicule 200 μm in diameter and 1.5 cm in length to a supercontinuum covering the visible spectrum down to 400 nm. Figure 5b shows that the observed spectrum of ultrashort pulses transmitted through a spicule considerably broadens upon increasing the spicule length.

Because the peak intensity of unfocused ultrashort pulses could achieve $\approx 7 \times 10^{10}$ W cm^{-2} in experiments, this resulted in the considerable enhancement of nonstationary processes such as transient spatial self-focusing and multiphoton ionization of the spicule material, and the short-wavelength edge of the supercontinuum shifted to 300 nm as the spicule length increased.

The simulation of the intensity spectral distribution of ultrashort light pulses in the 750–850-nm region transmitted through a spicule and its comparison with experimental data showed that the group velocity dispersion $\beta_2 = 2.8 \times 10^{-3}$ ps^2 m^{-1} for spicules is an order of magnitude lower than this dispersion in similar silica fibers, which is explained by the significant contribution from the wave-

guide part of dispersion due to the multilayer quasiperiodic structure of the cladding [15] compared to the contribution from the component caused by the spicule material.

4. Biosilicate nanocomposite materials and their nonlinear-optical properties

As mentioned in the Introduction, inorganic oxides are mainly synthesized by sol-gel chemistry methods [20]. Their synthesis is performed, as a rule, by using the two-stage introduction of biopolymers into a silicate matrix at the sol-gel transition stage; this process does not cause the mineralization of biomacromolecules. In Refs [19, 21], a new, one-stage method was proposed for the synthesis of biomimetic hybrid nanocomposite materials based on a silicon-containing tetraxis (2-hydroxyethyl) orthosilicate precursor (THEOS) (50%) and Na alginate (0.5–1%), Na hyaluronate (0.1–2%), and xanthane (0.5–2%) polysaccharides. This method does not involve the stage of sol solution formation that takes place in the conventional two-stage process.

In this case, the structure of the inorganic component of the nanocomposite material being produced is determined by a polysaccharide organic matrix, similarly to the formation of inorganic compounds in living organisms occurring due to their precipitation (biomineralization) on biomacromolecules serving as templates. In this connection, the mechanism of formation of such biosilicates resembles one of the mechanisms used by Nature for the synthesis of spicules.

By proceeding this process at a low temperature, we fabricated the samples of transparent biosilicate materials with transmission in the spectral range from 350 to 1400 nm virtually the same as that of the DSGS spicule material [19]. The refractive index of the synthesized materials was $n = 1.517$. The organic macromolecules contained in small concentrations in these materials play the role of a morphological matrix in the form of intricately intersected fibrils penetrating the entire material (Fig. 6a). The rest of the material volume is filled with spherical silicate particles (with an average diameter of 60 nm) deposited onto the organic matrix. Figure 6b gives a photograph of a transparent nanocomposite synthesized in an aqueous solution containing 50% of the THEOS precursor and 1% of sodium hyaluronate. The sample length is 15 mm [19].

The study of the interaction of unfocused ≈ 1-mJ femtosecond laser pulses (the laser beam diameter was 7 mm, and pulse repetition rate 100 Hz) with synthesized nanocomposite biomimetic media revealed that the nonlinear-optical parameters of these media were considerably higher than those for DSGS spicules [19]. The spectra of ultrashort pulses transmitted through xanthane, Na-alginate, and Na hyaluronate composite samples 10 mm in length demonstrate that the nonlinearity of the interaction of intense ultrashort pulses with these materials manifests itself much stronger (Fig. 6c). Here, the self-phase modulation of pulses caused by the Kerr nonlinearity of a medium and the self-focusing of pulses play the main role, which, together with other nonlinear-optical processes, leads to the formation of filaments in samples (Fig. 6b) and a supercontinuum. The best conversion efficiency of the pulse energy to a supercontinuum was achieved in sodium hyaluronate samples, for which higher energy levels were observed in supercontinuum spectrum (Fig. 6c). Sodium alginate samples proved to be optically unstable, while xanthane samples strongly absorbed ultrashort laser pulses.

A comparison of total supercontinuum energies P_{SC} generated in the spectral range from 400 to 650 nm in samples with the same geometry and different bioorganic additions (up to 1% in weight) revealed that P_{SC} for sodium hyaluronate samples was more than twice the P_{SC} for xanthane samples. The stable generation of a supercontinuum was observed in sodium hyaluronate samples even with a thickness as small as 1 mm. The approximate estimate of the nonlinear-optical coefficient of the sodium hyaluronate material based on the experimental study of the filamentation process in samples and data in paper [19] gives the value of $n_2 \approx 29 \times 10^{-14}$ cm^2 W^{-1}, which exceeds this coefficient for the DSGS spicule material by more than two orders of magnitude.

Another important feature of the supercontinuum generation in this material relates to the dependence of the total supercontinuum power P_{SC} on the concentration of

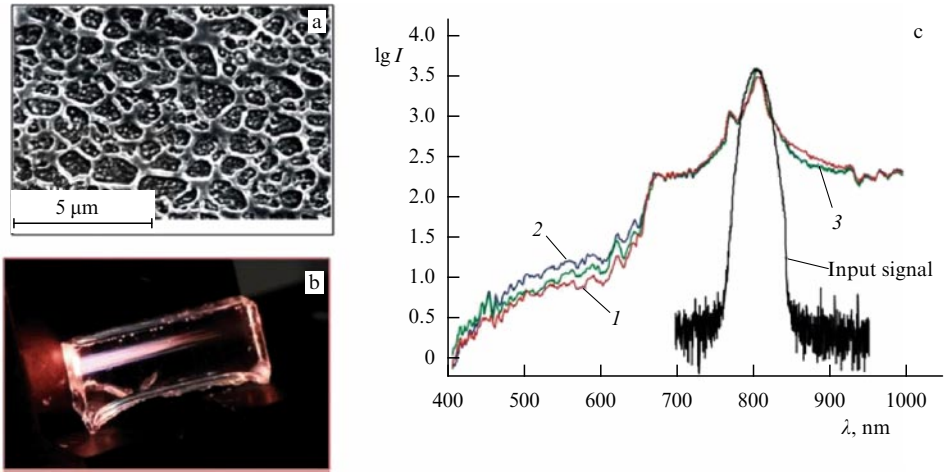

Figure 6. (a) SEM photograph of a section of an Na hyaluronate nanocomposite sample. (b) Photograph of an Na hyaluronate nanocomposite sample and a filament produced in it. (c) Supercontinuum spectra generated in nanocomposite materials based on the following complexes: THEOS (50%) + xanthane (0.5%) (curve *1*); THEOS (50%) + Na hyaluronate (0.25%) (curve *2*), and THEOS (50%) + Na alginate (0.25%) (curve *3*).

sodium hyaluronate polysaccharide and sample length [19], which allows one to control the nonlinear-optical parameters of the material itself and functional elements based on it.

5. Conclusion

The studies considered above have shown that the combination of proteins and polysaccharides created by Nature and self-organized with silicon dioxide extracted from sea water under natural conditions produced a unique nonlinear-optical biomineral nanocomposite material combining the flexibility and strength of a protein with the elasticity and strength of silicon dioxide, which is promising for applications in photonics. This process can be reproduced under artificial conditions using the adaptable sol-gel technology, which opens up a broad perspective for manufacturing new passive and active optoelectronic devices.

References

1. Churyumov G I, Maksimov I S, Ust'yantsev M A *Usp. Sovrem. Radioelektron.* (11) 35 (2005)
2. Meyers M A et al. *Prog. Mater. Sci.* **53** 1 (2008)
3. Müller W E G et al. *Biosensors Bioelectron.* **21** 1149 (2006)
4. Leys S P, Mackie G O, Reiswig H M *Adv. Marine Biol.* **52** 1 (2007)
5. Kulchin Yu N et al. *Vestn. Dal'nevost. Otd. Ross. Akad. Nauk* (1) 27 (2007)
6. Kulchin Yu N et al. *Opt. Memory Neural Networks* **16** 189 (2007)
7. Kulchin Yu N et al. *Kvantovaya Elektron.* **38** 51 (2008) [*Quantum Electron.* **38** 51 (2008)]
8. Galkina A N et al. *Khim. Fiz. Mezoskop.* **11** 310 (2009)
9. Voznesenskii S S et al. *Ross. Nanotekhnol.* **5** (1–2) 126 (2010) [*Nanotechnol. Russia* **5** (1–2) 142 (2010)]
10. Kulchin Yu N *Rare Met.* **28** (Special issue) 66 (2009)
11. Aizenberg J et al. *Proc. Natl. Acad. Sci. USA* **101** 3358 (2004)
12. Kul'chin Yu N et al. *Pis'ma Zh. Tekh. Fiz.* **34** (15) 1 (2008) [*Tech. Phys. Lett.* **34** 633 (2008)]
13. Kulchin Yu N et al. *Fotonika Biomineral'nykh i Biomimeticheskikh Struktur i Materialov* (Photonics of Biomineral and Biomimetic Structures and Materials) (Moscow: Fizmatlit, 2011)
14. Konorov S O et al. *Zh. Eksp. Teor. Fiz.* **123** 975 (2003) [*JETP* **96** 857 (2003)]
15. Kul'chin Yu N et al. *Opt. Spektrosk.* **107** 468 (2009) [*Opt. Spectrosc.* **107** 442 (2009)]
16. Maslov D V, Ostroumov E E, Fadeev V V *Kvantovaya Elektron.* **36** 163 (2006) [*Quantum Electron.* **36** 163 (2006)]
17. Agrawal G P *Nonlinear Fiber Optics* (San Diego: Academic Press, 1995) [Translated into Russian (Moscow: Mir, 1996)]
18. Kulchin Yu N et al., in *Biosilica in Evolution, Morphogenesis, and Nanobiotechnology* (Eds W E G Müller, M A Grachev) (Berlin: Springer, 2009) p. 315
19. Kulchin Yu N et al. *Laser Phys.* **21** 630 (2011)
20. Dunn B et al. *Acta Mater.* **46** 737 (1998)
21. Shchipunov Yu A, in *Perspektivnye Napravleniya Razvitiya Nanotekhnologii v DVO RAN* (Promising Directions in the Development of Nanotechnologies at the Far Eastern Branch, Russian Academy of Sciences) Vol. 2 (Executive Ed. Yu N Kulchin) (Vladivostok: Dal'nauka, 2009) p. 157

PACS numbers: 37.10.De, 37.10.Gh, 32.30.Jc
DOI: 10.3367/UFNe.0181.201108j.0896

Laser cooling of rare-earth atoms and precision measurements

N N Kolachevsky

1. Introduction

Today, the physics of microwave and optical frequency standards is one of the most rapidly advancing lines of inquiry. Progress here can be readily quantitatively evaluated: while in the early 2000s the problem of reaching a measurement inaccuracy at a level of 10^{-15} was considered [1], now systems capable of generating highly stable signals with a fractional inaccuracy better than 10^{-17} are being developed [2].

The improvement in frequency stability opens new possibilities for solving problems of time and frequency metrology, global positioning and navigation, geodesy, gravimetry, and the sensitive testing of fundamental physical theories. The solution to these problems at the modern level of precision requires the practical realization of new principles of generating time and frequency signals on Earth surface and in space. In 2014, the orbital launching of ACES (Atomic Clock Ensemble in Space) is planned, which constitutes an ensemble of high-precision microwave atomic clocks with an inaccuracy of a few digits in the 16th decimal place [3]. Simultaneously, methods are being developed for transmitting extremely stable signals via both conventional microwave channels and optical communication lines [4]. Precise time and frequency signals are required in numerous fundamental and applied problems, making this research field one of the most urgent issues in modern physics.

A considerable improvement in the accuracy of frequency standards has been achieved mainly due to advances in the development of optical clocks operating in the frequency range close to $\nu_0 \sim 10^{15}$ Hz. The increase in the carrier frequency compared to microwave standards ($\nu_0 \sim 10^{10}$ Hz) for the same spectral linewidth $\delta\nu$ has led to an increase in the resonance quality factor $Q = \nu_0/\delta\nu$ and a corresponding decrease in the inaccuracy. To excite and detect narrow optical transitions (the typical width today is $\delta\nu \sim 1$ Hz), it is necessary to solve a number of problems: (i) to create stable laser systems emitting lines with spectral widths smaller than 1 Hz; (ii) to search for optimal atomic and ion systems providing the best metrological characteristics, and (iii) to develop methods for cooling atoms and for exciting and interrogating resonances providing the ultimate accuracy.

Recent advances in the stabilization of lasers have proved to be so significant (see review [5]) that these light sources have become a reliable tool accessible to any laboratory in the

N N Kolachevsky Lebedev Physical Institute, Russian Academy of Sciences, Moscow, Russian Federation;
Moscow Institute of Physics and Technology (State University), Dolgoprudnyi, Moscow region, Russian Federation
E-mail: kolik@lebedev.ru

Uspekhi Fizicheskikh Nauk **181** (8) 896 – 903 (2011)
DOI: 10.3367/UFNr.0181.201108j.0896
Translated by M Sapozhnikov; edited by A Radzig

world. At the same time, the question of the choice of optimal metrological transitions remains open to a certain degree, and now quite different atomic systems and different interrogation methods are being extensively investigated. We shall exemplify clocks based on single ions [2], which offer the indisputable advantage of the almost perfect isolation of ions from external interactions, and optical lattice clocks based on neutral atoms [6], which provide high long- and mid-term stability due to the large number of interrogated atoms.

In this report, rare-earth atoms with the open 4f electron shell (such as Pr, Nd, Dy, Er, Tm) are discussed as potential candidates for use in optical clocks. To create an optical clock, it is necessary to resolve the following issues: to provide a low temperature of atoms, to isolate them from the environment, and to provide a long interaction time with the exciting laser field. These problems are gotten around using the laser cooling method, its applicability to a certain atom requiring a separate careful study. In 2009, the laser cooling of a thulium atom was demonstrated for the first time at the Laboratory of Optics of Active Media at the Lebedev Physical Institute, RAS (FIAN in *Russ. abbr.*). The report presents the review of recent results obtained by researchers at the FIAN laboratory and by students and postgraduates at the Moscow Institute of Physics and Technology (MIPT).

The paper outline is as follows. The possibility of utilizing the intrashell magnetic dipole 4f–4f transitions in a thulium atom for optical frequency standards is analyzed in Section 2. In Section 3, the review of basic results on the laser cooling of thulium and its magneto-optical trapping is presented. Section 4 is devoted to the study of the sub-Doppler cooling of thulium and its magnetic dipole trapping.

2. Transitions between fine-structure sublevels of a ground-state thulium atom

A specific feature of the ground state of rare-earth atoms with the open 4f shell is the presence of the fine structure: depending on the quantum number of the total electron momentum J, determined by the mutual orientation of electron momenta in the 4f shell, the ground state is split into a number of fine-structure sublevels. In this case, the 4f shell is located inside the closed outer $5s^2$ and $6s^2$ shells, providing the screening of fine-structure sublevels by outer shell electrons.

In 1986, Aleksandrov et al. [7] pointed out for the first time the possibility of employing optical transitions between the ground-state fine-structure components as metrological transitions because the electron screening considerably reduces the sensitivity to atomic collisions with a buffer gas. Later on, the screening in collisions with He atoms was quantitatively examined in experiments [8] and confirmed by calculations [9, 10]. As this takes place, the ratio of elastic and inelastic collision cross sections for ground-state Tm atoms is of order 5×10^4 (see paper [10] and references cited therein).

In 1999, it was proposed at the Laboratory of Optics of Active Media (FIAN) to use the magnetic dipole $4f^{13}6s^2\,(J = 7/2) \rightarrow 4f^{13}6s^2\,(J = 5/2)$ transition in a thulium atom at a wavelength of 1.14 μm with a spectral width of 1.1 Hz (see Fig. 1) as a promising candidate for optical clocks (some parameters of this transition are presented in paper [11]). This idea was supported by I I Sobel'man and the study of rare-earth atoms was initiated at the Laboratory. First, it was assumed that in the presence of screening it is appropriate to excite the metrological transition in a dense

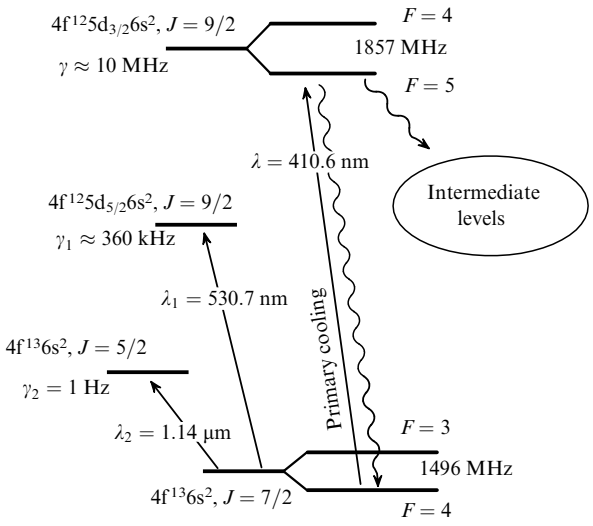

Figure 1. Energy level diagram of the ^{169}Tm atom. Shown are the ground-state fine structure (the $4f^{13}6s^2$ configuration), hyperfine-structure components, and atomic energy levels used for the primary and secondary laser cooling at wavelengths of 410.6 and 530.7 nm, respectively.

laser-cooled cloud of thulium atoms, which can provide the high short-term stability of a standard. However, in 2010 researchers at Harvard University (USA) found in experiments that the screening effect disappeared in collisions between Tm atoms in certain spin states [12], which complicates the construction of an optical clock based on a dense atomic cloud.

More promising is an idea underlying the estimate of the differential polarizability of the $J = 7/2$ and $J = 5/2$ ground-state levels in thulium [13]. The scalar polarizability of the $J = 7/2$ ground state of thulium is $\alpha_s = 161$ atomic units (a.e.) [9] and is comparable with the polarizability of the ground state, for example, of rubidium (319 a.e.). The analysis of the fine structure of a thulium atom points to the fact that polarizabilities for the $J = 7/2$ and $J = 5/2$ fine-structure components in the ground state should be close: allowed transitions from each of the ground-state sublevels $4f^{13}6s^2\,(J = 7/2)$ and $4f^{13}6s^2\,(J = 5/2)$ have close wavelengths and oscillator strengths. The structure of even terms in thulium is split into two virtually identical branches separated by an interval of about 8800 cm^{-1}, corresponding to the ground-state fine splitting. Each of the branches has its own ionization threshold. The allowed transitions from the odd $4f^{13}6s^2\,(J = 7/2)$ and $4f^{13}6s^2\,(J = 5/2)$ levels to the corresponding components of these branches are also identical to a great extent, resulting in the identical polarizabilities of the ground-state levels.

The detailed calculation of the differential polarizability is time-consuming [13] and has not been performed to date. However, if we admit that the assumption of a low differential polarizability is correct, a new outlook opens for using the 1.14-μm magnetic dipole transition in optical clocks.

One of the possibilities resides in the localization of thulium atoms in the antinodes or nodes of a standing light wave (optical lattice), as is realized in optical clocks based on strontium and ytterbium atoms (see, for example, paper [6] and references cited therein). In this case, the contribution of the Doppler effect is suppressed (the Lamb–Dicke regime) and the interaction between atoms is eliminated. However, it is necessary to take into account the dynamic Stark shift

caused by the optical lattice itself. In the case of Sr, the wavelength of the optical lattice is carefully selected, so that the dynamic Stark shifts of the upper and lower metrological levels would be the same (the 'magic' wavelength [14]). For the 1.14-μm transition in a thulium atom, any wavelength will be in fact 'magic', because the polarizabilities of the levels are identical. This considerably alleviates the problem of loading atoms into the lattice and allows one to work in a convenient spectral range.

Another important consequence can be suppression of the frequency shift caused by the black body radiation. Today, it is this effect that mainly restricts the accuracy of optical lattice clocks based on Sr atoms [15]. Because this effect is simply reduced to the dynamic Stark shift caused by broadband radiation of heated surrounding bodies, the coincidence of polarizabilities of metrological levels will result in its suppression.

So far, direct precision spectroscopy of magnetic dipole transitions between the fine-structure sublevels in ground-state rare-earth atoms has not been performed. The problems discussed in this section require the experimental verification and detailed quantitative estimate. We assume that the 1.14-μm magnetic dipole transition of a thulium atom is not inferior in its basic metrological characteristics to clock transitions in Sr and Yb atoms, which have found wide applications in optical clocks with a fractional inaccuracy of order 10^{-16}.

In turn, to perform precision measurements and to load atoms into optical traps, temperatures lower than 10 μK are required, which can be achieved only by the laser cooling method. In our country, laser cooling is being actively studied by research groups at the Institute of Spectroscopy, RAS, where cold rubidium atoms are investigated [16]; at the Institute of Laser Physics, SB RAS, where the use of laser-cooled magnesium atoms for frequency standard problems is planned [17]; at the Institute of Semiconductor Physics, RAS, where cold Rydberg rubidium atoms are studied [18]; at the Institute of Applied Physics, RAS, where the two-dimensional lithium Fermi condensate was produced [19], and at the All-Russian Research Institute of Physicotechnical and Radio Engineering Measurements, where several cesium fountains are working [20] and an optical clock built around Sr atoms is being developed. In Section 3, the original results of studies on the laser cooling of thulium atoms, pursued at FIAN, are presented.

3. Magneto-optical trap for thulium atoms

3.1 Laser cooling of new atomic ensembles

The laser cooling method opened fundamentally new possibilities in the fields of precision laser spectroscopy [21], the investigation of particle collisions [22], atomic interferometry, and the production of quantum condensates [23]. This method is not universal because the efficient laser cooling of an atom can be achieved if the following requirements are fulfilled: (i) the atom should have a cyclic transition in the optical (UV) spectral range; (ii) the transition should be strong enough (the transition probability $A \sim 10^8$ s^{-1}) to provide the high cooling rate, and (iii) a laser with high enough power ($P \sim 1$ mW), being tuned to resonance with this transition, is needed.

At present, laser cooling and trapping in magneto-optical traps (MOTs) have been achieved for all alkali and alkali-earth atoms, as well as metastable-state noble gas atoms (except for radon). The possibility of laser cooling and trapping of atoms from the rest of the Periodic Table is being extensively investigated. In recent years, the laser cooling and trapping of the Hg [24], Cd [25], and some other atoms in MOTs have been demonstrated. The use of new ultracold atomic ensembles is planned for solving problems in metrology, quantum informatics, investigations of particle collisions, and testing fundamental physical theories. For example, an important unsolved problem is the efficient laser cooling of hydrogen (antihydrogen) atoms, which will allow one to compare the spectra of matter and antimatter with a high resolution and perform sensitive tests of the *CPT* theorem. This problem became even more urgent after the successful synthesis and trapping of antihydrogen atoms in a magnetic trap [26].

Aside from the metrological applications discussed in Section 2, laser-cooled rare-earth atoms are of great interest for the problems of quantum condensates and studies of molecular structures. The magnetic moment of these atoms in the ground state is many times higher than that of alkali atoms. This moment for a Tm atom is $4\mu_B$, and for Dy, for example, amounts to $10\mu_B$ (μ_B is the Bohr magneton), which opens wide possibilities for studying the magnetic interactions of atoms with superconductors [27] and dipole–dipole interactions [28]. The possibility has appeared of synthesizing cold polar molecules [29] having a magnetic moment (for example, TmRb).

In the last few years, the laser cooling of the two representatives of rare-earth elements with an open 4f shell, erbium [30] and dysprosium [31], has been achieved in the USA. In turn, in our laboratory at FIAN we have demonstrated the laser cooling of thulium atoms [32, 33]. The laser cooling of rare-earth atoms is complicated due to the absence of strong cyclic transitions from the ground state. Because of a great number of intermediate energy levels, there always exists a probability of depopulation from the cooling cycle, which cannot be 'shut off' by repumping lasers, as, for example, in rubidium. The calculation of transition probabilities in these atoms is rather inaccurate and can give only rough estimates of the decay probability.

3.2 Cooling and magneto-optical trapping of thulium atoms

Earlier, we investigated optical transitions in a thulium atom convenient for laser cooling [11]. Thulium possesses the only stable isotope ^{169}Tm with the nuclear spin $I = 1/2$ (bosonic isotope). Therefore, each its energy level will be spit into two hyperfine-structure sublevels. It was proposed to utilize the strong, almost cyclic $4f^{13}6s^2$ ($J=7/2$, $F=4$) $\rightarrow$ $4f^{12}5d6s^2$ ($J = 9/2$, $F = 5$) transition at 410.6 nm with the natural width $\gamma = 10.0(4)$ MHz (see Fig. 1). Here, F is the quantum number of the total atomic moment. Despite the decay of the upper cooling level to intermediate energy levels of the opposite parity (indicated in Fig. 1 as 'intermediate levels'), in 2009 we managed to demonstrate the efficient Zeeman cooling of a hot Tm atomic beam [32].

A schematic of a setup for laser cooling and magneto-optical trapping of thulium atoms is depicted in Fig. 2. A magneto-optical trap represents a classical setup of three pairs of mutually orthogonal circularly polarized cooling laser beams emitting at frequencies tuned to the red region of the spectrum with respect to the atomic optical transition. The atoms are trapped in a stainless steel vacuum chamber

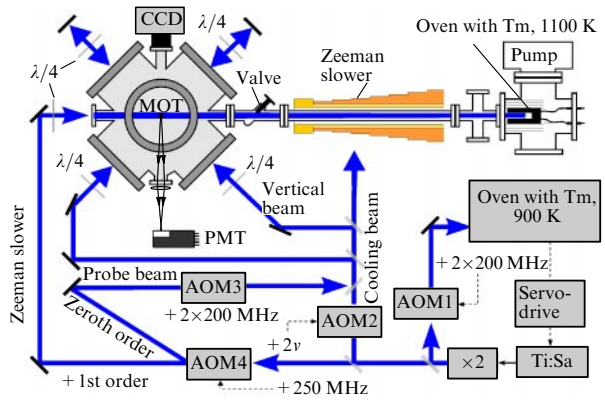

Figure 2. Schematic of the setup for laser cooling of thulium atoms: AOM — acoustooptic modulator; PMT — photomultiplier, and CCD — charge-coupled device.

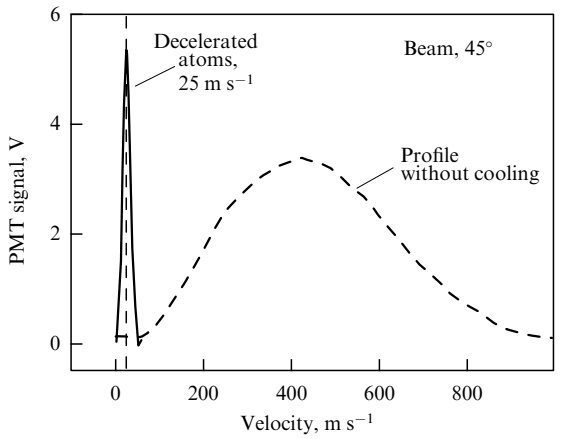

Figure 3. Illustration of the operation of a Zeeman slower for an atomic thulium beam. The dashed curve fits the velocity distribution of thulium atoms for the switched-off moderator. The distribution corresponds to temperature 1100 K. The solid curve is the low-velocity part of the distribution for the operating moderator.

with optical windows for three orthogonal axes for cooling beams and two additional axes at an angle of 45° for loading and detecting. The chamber is evacuated down to less than 10^{-8} mbar with an ion-getter pump 30 l s^{-1} in capacity. At the center of the chamber, a quadrupole magnetic field on the order of 10 G cm^{-1} is produced with the help of coils in the anti-Helmholtz configuration. The laboratory magnetic field is compensated for by additional coils.

We used in experiments the second harmonic of a cw Ti:sapphire laser at a wavelength of 410.6 nm. The laser frequency was stabilized by a saturated absorption signal generated in the second oven with thulium vapor at 900 K [11]. The second-harmonic frequency was shifted in several acoustooptic modulators to produce three light fields at different frequencies: (1) a light field for a Zeeman slower with frequency detuned by −150 MHz with respect to the frequency of the $F = 4 \rightarrow F = 5$ cooling transition (see Fig. 1); (2) a cooling field with the frequency detuning from the resonance variable in the range from -0.5γ to -4γ, and (3) a probe field tuned exactly to resonance with the cooling transition. A computer-aided digital controller was used to generate pulse trains for all three light fields.

Thulium atoms were loaded from a beam formed in a sapphire oven heated to 1100 K using a system of apertures. This temperature is considerably lower than the thulium melting point (1818 K). However, the metal is efficiently sublimated from a surface, the pressure of saturated thulium vapor at 1100 K being 10^{-2} mbar. The oven volume is evacuated with a turbomolecular pump (30 l s^{-1}) down to 10^{-7} mbar.

The atomic beam was decelerated by a counter light field in a Zeeman slower 40 cm in length producing a longitudinally inhomogeneous magnetic field compensating for the Doppler shift changing during the deceleration of atoms. It was shown in paper [32] that the slower decelerates ~ 1% of the atoms entering the main chamber to a velocity of 25 m s^{-1}. The velocity distribution of atoms with the switched-off field of the cooler and the low-velocity part of the distribution for the switched-on slower are presented in Fig. 3. In this case, we detected the luminescence signal of atoms excited by the laser field at an angle of 45° to the atomic beam direction. The measurement was performed with a PMT by scanning the probe laser beam frequency, which was followed by the recovery of the atomic velocity distribution. Estimates show that the flux of cold ions at the central part of the vacuum chamber is 10^7 s^{-1} cm^{-2} and has a cross section of about 1 cm^2.

3.3 Lifetime of atoms in a magneto-optical trap

A cloud of cooled atoms produced in the intersection region of cooling beams had a regular shape, a Gaussian distribution of the luminescence intensity, and a characteristic radius of 80 μm (1/e). We measured the basic characteristics of a thulium MOT: the number, lifetime, and temperature of the atoms [33].

To determine the number of atoms in the MOT, we detected the luminescence of the cloud atoms excited by photons of the cooling beams. The luminescence signal was measured with a PMT operating in the current regime (see Fig. 2). The number of trapped atoms could be varied in the range from 10^2 to 10^7, depending on the intensity and frequency detuning of cooling beams and the atomic beam intensity.

The dynamics of the number of atoms in the MOT is governed by the following equation [22]

$$\frac{\mathrm{d}N}{\mathrm{d}t} = R - \Gamma N - \beta N^2, \qquad \beta = \frac{\sigma'}{2\sqrt{2}\,\pi^{1.5} r^3}, \tag{1}$$

where R is the atom trapping rate in the MOT, Γ is the linear loss coefficient (reciprocal to the lifetime), β is the quadratic loss coefficient, r is the cloud radius at the 1/e level, and $\sigma' = \langle v\sigma \rangle$ is the rate constant of binary atomic collisions. If the MOT loading is terminated at the instant of time $t = 0$ ($R_{t<0} \neq 0$, $R_{t>0} = 0$), the number of trapped atoms will decrease by the law

$$N(t) = \frac{N_0 \exp(-\Gamma t)}{1 + \beta N_0 \Gamma^{-1} \left[1 - \exp(-\Gamma t)\right]}. \tag{2}$$

In turn, the loading curve ($R_{t<0} = 0$, $R_{t>0} \neq 0$) will be described by the expression

$$N(t) = \frac{1}{2\beta}\left[-\gamma + \sqrt{\gamma^2 + 4\beta R}\,\tanh\left(\frac{t+c}{2}\sqrt{\gamma^2 + 4\beta R}\right)\right], \tag{3}$$

where c is the constant determined from the condition $N(0) = 0$. By neglecting binary collisions, expression (2) is simplified:

$$N(t) = N_0 \exp(-\Gamma t), \quad (4)$$

where N_0 is the initial number of atoms. Obviously, the loading process in this case will also be described by an exponential with the same time constant.

The linear loss coefficient comprises two terms: $\Gamma = \Gamma_0 + \Gamma_1$. The first term Γ_0, related to collisions of atoms in the MOT with residual gas in the vacuum chamber, is independent of the cooling radiation intensity. The second term Γ_1 is related to the decay of the upper energy level of the cooling transition to other levels (see Fig. 1). This term depends on the upper-level population and, hence, on the intensity of cooling beams.

The exact solution to the problem requires the consideration of many intermediate atomic energy levels and unknown transition probabilities. By using theoretical estimates [11] predicting a small value of the branching ratio on the order of 10^{-5}, we considered the simplified two-level model in which an excited atom can irrevocably leave the cooling cycle with the probability $k\gamma$ (k is the unknown branching ratio). The linear loss coefficient in this model takes the form

$$\Gamma = \tau^{-1} = \Gamma_0 + \Gamma_1 \frac{N_2}{N} = \Gamma_0 + \frac{\Gamma_1}{2} \frac{S}{1 + S + 4\delta^2}, \quad (5)$$

where $S = I/I_{\text{sat}}$ is the saturation parameter, $I_{\text{sat}} = \pi hc/3\lambda^3\tau = 18.9$ mW cm^{-2} is the transition saturation intensity (here, λ is the cooling transition wavelength, and τ is the upper-level lifetime), and δ stands for the detuning from the resonance in units of γ.

We determined the branching ratio by measuring the dependence of the lifetime τ on the intensity of cooling beams (the saturation parameter S). The measurements were performed for a relatively small number of trapped atoms (10^5) and the cloud radius of order 100 μm. The experiments showed that binary atomic collisions under such conditions are insignificant [33], and simplified model (4) can be applied.

The lifetime was measured by the decay curve of the trap after switching off loading. The loading was terminated by switching off the Zeeman slower. The time dependence of luminescence of atoms in the MOT, detected with a PMT, was approximated by the model expression (4). Figure 4 presents the dependence of the lifetime of atoms in the MOT on the power of cooling beams for three values of the frequency detuning. By approximating the data using expression (5), we obtained the probability for the upper-level decay: $\Gamma_1 \geqslant 22(6)$ s^{-1}. The inequality sign appears here because a part of the population from intermediate atomic energy levels can return to the cooling cycle, and therefore we can give only the lower bound for Γ_1. The branching ratio $k \geqslant 3.5 \times 10^{-7}$ corresponds to this value of Γ_1, which does not contradict calculations [11].

As the concentration of atoms in the MOT increases, binary particle collisions begin to play a noticeable role. This is confirmed by the fact that the experimental unloading curve is already poorly described by approximate expression (4), and exact expression (2) should be used for trap unloading, and expression (3) for trap loading. Fitting curves at the concentration of atoms at the trap center equal to 10^{12} cm^{-3} are compared in the inset to Fig. 4.

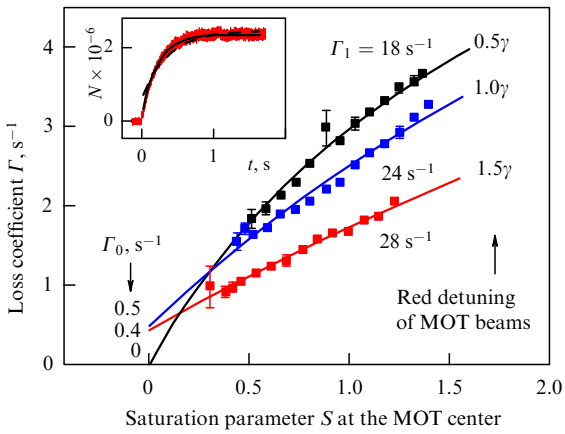

Figure 4. Dependences of the loss coefficient Γ on the cooling beam intensity for three red detunings. The data are approximated by expression (5). Measurements were performed for a small number of atoms in a trap (10^5) when the role of binary collisions is negligible. The inset shows the trap loading curve for a large number of atoms (2×10^6) in the MOT. The dashed curve is the exponential fit, and the solid curve is the fit by expression (3).

We estimated the rate constant of binary collisions of thulium atoms in the MOT as $\sigma' = 3(2) \times 10^{-10}$ cm^3 s^{-1}. Collisions in the operating MOT occur between both ground-state and excited atoms, the cross sections for these collisions being considerably different. Nevertheless, the rate constant σ' is close to the value 10^{-10} cm^3 s^{-1} obtained in paper [12] where Tm–Tm collisions between spin-polarized ground-state atoms confined in a magnetic trap were studied.

4. Sub-Doppler cooling and a magnetic trap

4.1 Doppler and sub-Doppler cooling mechanisms

The final temperature that can be achieved upon laser cooling of atoms is determined by a balance between the cooling and heating rates, which appears during absorption and reemission of cooling laser radiation. According to book [34], the Maxwell velocity distribution of atoms is formed in the stationary regime, which allows the use of such a parameter as the cloud temperature T.

Initially, the *Doppler* theory of laser cooling for a two-level atom was developed [35]. In the approximation of $I < I_{\text{sat}}$, the final temperature of cooled atoms in the Doppler theory depends on the red frequency detuning δ (in units of γ) of cooling radiation from the resonance as

$$T(\delta) = \frac{h\gamma}{2k_{\text{B}}} \frac{\delta^2 + 1/4}{\delta}, \quad (6)$$

where k_{B} is the Boltzmann constant. This temperature has a minimum at $\delta = 1/2$, which is called the Doppler limit:

$$T_{\text{D}} = \frac{h\gamma}{2k_{\text{B}}}. \quad (7)$$

For the 410.6-nm transition in a thulium atom, $T_{\text{D}} = 240$ μK. This temperature is too high for solving the problem of trapping atoms in an optical lattice or detailed studies of particle collisions in the quantum regime. The necessity appears to apply other methods to lower the temperature, for example, *sub-Doppler* cooling.

For atoms with the nondegenerate structure of magnetic sublevels in the ground state (in particular, ^{169}Tm), additional mechanisms are involved which cause the increase in cooling rate and temperature lowering [36]. The minimal temperature achieved by sub-Doppler cooling approaches the *recoil limit* $T_{\rm rec} = h^2/(2\lambda^2 m k_{\rm B})$, which is usually considerably lower than the Doppler limit (m is the atomic mass). For the 410.6-nm transition in thulium, this limit is 330 nK.

For sub-Doppler cooling on $F \to F+1$ fine-structure transitions (F is the total momentum of the atom), the final atomic temperature depends on the detuning δ and light field intensity I as [37]

$$T \propto \frac{I}{F\delta}\,. \tag{8}$$

Unlike temperature (6) in the Doppler theory, which passes minimum (7), the atomic temperature in the sub-Doppler regime monotonically decreases upon increasing the frequency detuning δ.

The sub-Doppler cooling mechanism is very sensitive to a magnetic field [38–40]. In the absence of a magnetic field, the Doppler and sub-Doppler cooling mechanisms efficiently operate together. However, in the presence of a magnetic field B, the Doppler force is zero for atoms with the velocity

$$v_{\rm D} = -g_{\rm e}\frac{\mu_{\rm B}B}{\hbar k}\,, \tag{9}$$

while the sub-Doppler force is zero for atoms with the velocity

$$v_{\rm S} = -g_{\rm g}\frac{\mu_{\rm B}B}{\hbar k}\,, \tag{10}$$

where $g_{\rm e}$ and $g_{\rm g}$ are the Landé splitting factors for the upper and lower cooling levels, and k is the wave number. In this case, sub-Doppler cooling involves only a small velocity range around $v_{\rm S}$. If velocities $v_{\rm D}$ and $v_{\rm S}$ considerably differ, only a small group of atoms are subjected to sub-Doppler cooling, which does not affect in fact the total cloud temperature. As the magnetic field is increased, the difference between velocities $v_{\rm D}$ and $v_{\rm S}$ also increases, which leads to the actual cessation of sub-Doppler cooling in alkali atoms already in magnetic fields of order 1 G [41].

This effect prevents the achievement of sub-Doppler temperatures directly in a MOT because, due to the finite size of the cloud and the adjustment inaccuracy, the cloud of cold atoms is collected not exactly at the zero point of the quadrupole magnetic field in the MOT. Because of this, a special cycle of sub-Doppler cooling is invoked in most experiments, when the quadrupole magnetic field in the MOT is switched off, the frequency detuning is increased, and the laser radiation intensity is decreased.

However, as follows from formulas (9) and (10), the efficient sub-Doppler cooling of atoms inside a MOT can be observed when the Landé g factors for the upper and lower cooling levels coincide [42]. For the 410.6-nm cooling transition in a thulium atom, the relative difference of g factors is only 2%, which provides efficient sub-Doppler cooling directly in the MOT.

4.2 Temperature of atoms in a magneto-optical trap

The cloud temperature was determined by the scattering of atoms after switching off the light and magnetic fields in a MOT (the ballistic scattering method). Within time Δt after switching off the fields, the cloud was illuminated by a short 200-μs probe laser pulse tuned exactly to the resonance of the cooling transition (see Fig. 1). Photographs of the atomic cloud obtained within different time intervals after switching off the fields are presented in Fig. 5a.

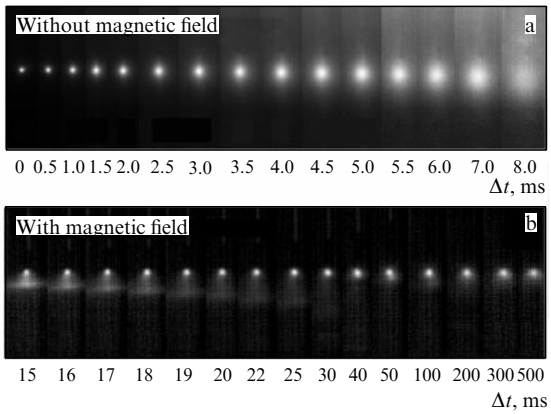

Figure 5. (a) Successive photographs of atoms flying apart in the ballistic regime in a MOT in the absence of a quadrupole magnetic field. The corresponding time intervals Δt are indicated in the figure. (b) Images of the cloud in a quadrupole magnetic field. The bright point shows magnetically trapped atoms; the elliptic cloud of untrapped atoms falling under the action of gravity is also observed.

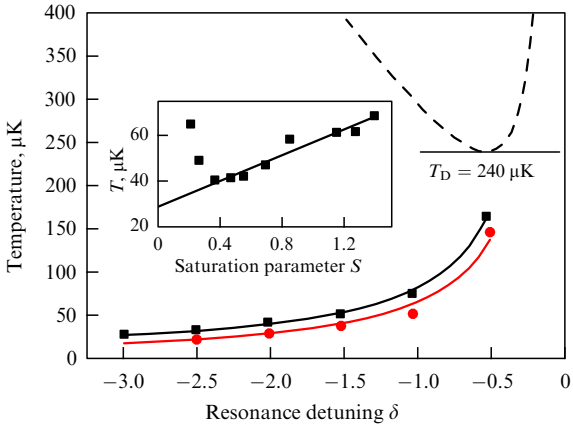

Figure 6. Dependence of temperature T on the frequency detuning δ of cooling radiation for radiation intensities $S = 2$ (squares) and 0.4 (circles). The dashed curve corresponds to the Doppler theory (6). The inset shows the dependence of temperature (squares) on the radiation intensity at the MOT center; the straight line is a linear fit of data for $S > 0.5$.

Assuming the Maxwell velocity distribution of atoms, the dependence of the cloud radius r (at the 1/e level) on the delay time Δt takes the form

$$r(\Delta t) = \sqrt{r^2(0) + \frac{2k_{\rm B}T}{m}\,\Delta t^2}\,. \tag{11}$$

Figure 6 depicts the dependence of the temperature of atoms on the frequency detuning of cooling beams, measured according to formula (11). The temperature decreases monotonically upon increasing the frequency detuning modulus, which suggests that sub-Doppler cooling dominates. For comparison, the dashed curve in Fig. 6 shows dependence (6) corresponding to the Doppler theory. As mentioned above, the high efficiency of sub-Doppler cooling in our case is determined by the close values of the Landé $g_{\rm g}$ and $g_{\rm e}$ factors of thulium energy levels involved in the cooling

process. The lowest detected temperature in the MOT was 25(5) μK.

The dependence of the temperature of atoms on the power of cooling beams is shown in the inset to Fig. 6. At low radiation intensities, the trap becomes unstable, resulting in the increase in temperature. At higher radiation powers, temperature increases linearly according to formula (8). The linear extrapolation leads to nonzero temperature at zero power, attesting the existence of an additional heating channel, which can be related to the inaccurate coincidence of the Landé g_e and g_g factors.

4.3 Magnetic trap

Ground-state thulium atoms possesses a large magnetic moment equal to $4\mu_B$. Due to the interaction of this moment with the quadrupole magnetic field of a MOT and due to low sub-Doppler temperatures in the latter, part of the atoms can be captured in a *magnetic trap* (MT). The atomic potential in such a trap is described by the expression

$$U(x, y, z) = \mu\sqrt{x^2 b_x^2 + y^2 b_y^2 + z^2 b_z^2} + mgz\,, \qquad (12)$$

where μ is the effective magnetic moment of the atom, b_i is the magnetic field gradient along the ith axis, m is the atom mass, and g is the acceleration of gravity.

To study the MT, we performed experiments similar to temperature measurements, but with the switched-on quadrupole field of the MOT. Figure 5b gives a number of images recorded under such conditions. By comparing the atoms flying apart in the MOT in Figs 5a and 5b, we see that a fraction of the atoms from the MOT is confined in the MT for a long time, up to 0.5 s, whereas in the absence of the quadrupole field the atoms fly apart for about 10 ms. The photographs in Fig. 5b also show the image of atoms that are not confined in the magnetic trap and fall under the action of gravity.

The spatial profile of the MT is not Gaussian, and for this reason the temperature was estimated by the method described in paper [42]. Measurements give the temperature of atoms in the MT from 15 to 50 μK, depending on the initial temperature of atoms in the MOT. It is expected that the temperature of atoms in the MT should be approximately 1/3 of the temperature of atoms in the MOT [43], which is confirmed by experimental results.

5. The outlook

To study metrological characteristics of the 1.14-μm transition in a thulium atom and collisions of atoms in the quantum regime, we plan to load atoms into an optical dipole trap or an optical lattice. The second harmonic of a neodymium laser at 532 nm can be used as radiation for the optical trap. In this case, red detuning from the resonant 530.7-nm transition (see Fig. 1) and all other strong transitions in the blue spectral region is realized. Estimates show that for 2 W of radiation power and focusing to a waist 25 μm in radius, the trap depth corresponds to a temperature of 30 μK. The optical trap opens the possibility of studying collisions between atoms in different spin states, scattering cross sections in different magnetic fields (Feshbach resonances), and characteristics of the metrological transition discussed in Section 2. However, to perform reliable loading into the optical trap, it is desirable to achieve a temperature lower than 10 μK.

To reduce the temperature, we plan to realize the secondary cooling cycle on the weaker, completely cyclic 530.7-nm $4f^{13}6s^2\,(J = 7/2) \rightarrow 4f^{12}5d_{5/2}6s^2\,(J = 9/2)$ transition with a natural linewidth of 360 kHz (see Fig. 1). In so doing, the Doppler limit is reduced to 9 μK. Taking into account that the Landé g factors for the corresponding energy levels are also close, we expect a further decrease in temperature due to sub-Doppler mechanisms. This transition can be excited by the second harmonic of a frequency-stabilized semiconductor laser. Thus, we can anticipate the capture of a few million atoms at a temperature of order 1 μK, followed by their loading into an optical trap or lattice.

We also plan in parallel to construct a subhertz laser for exciting the 1.14-μm clock transition. The laser will be stabilized with respect to a vibration- and temperature-compensated resonator, as described in review [5]. The transition will be detected by a luminescence signal from the strong 410.6-nm transition, which is sensitive to the ground-state depopulation.

6. Conclusions

Analysis of the latest studies on the laser cooling of rare-earth atoms and the possibility of using them in precision spectroscopy and metrology and for studying their interactions in the quantum regime has shown that, due to the specific structure of the electron shells in Tm, the 1.14-μm magnetic dipole transition in a thulium atom can be of considerable interest for the development of a new optical clock with high short-term stability.

We have constructed a magneto-optical trap for thulium atoms and studied their laser cooling at a wavelength of 410.6 nm. The lifetime of atoms in the trap has been measured and the decay constant of the upper cooling level has been determined. It has been shown that, owing to the unique energy level diagram, sub-Doppler cooling is observed directly in the MOT without utilizing a special additional cycle. The lowest temperature achieved in the MOT is 25(5) μK for the number of atoms equal to 3×10^6 and the cloud radius of 80 μm, which corresponds to the phase density $\rho = 10^{-5}$.

Our studies have shown that the further cooling of thulium atoms to 1 μK is also possible, which is required for the loading of atoms into an optical trap or an optical lattice formed by a standing light wave.

Acknowledgments

The author expresses deep appreciation to all the participants in the project on laser cooling of thulium: V N Sorokin, S I Kanorsky, A V Akimov, A V Sokolov, K A Chebakov, and D D Sukachev, whose studies were used in this paper. Special thanks are due to G A Mesyats and A V Masalov for their constant support of the project.

This work was supported by DFG (grant No. 436Rus 113/984/0-1), the Presidential grant for young scientists, MD-669.2011, and the Program of Fundamental Studies: Extremal Light Fields and Their Applications, of the RAS Presidium.

References

1. Kolachevsky N N *Usp. Fiz. Nauk* **174** 1171 (2004) [*Phys. Usp.* **47** 1101 (2004)]
2. Chou C W et al. *Phys. Rev. Lett.* **104** 070802 (2010)

3. Cacciapuoti L et al. *Nucl. Phys. B Proc. Suppl.* **166** 303 (2007)
4. Grosche G et al. *Opt. Lett.* **34** 2270 (2009)
5. Kolachevsky N N *Usp. Fiz. Nauk* **178** 1225 (2008) [*Phys. Usp.* **51** 1180 (2008)]
6. Blatt S et al. *Phys. Rev. Lett.* **100** 140801 (2008)
7. Aleksandrov E B et al. *Opt. Spektrosk.* **54** 3 (1983) [*Opt. Spectrosc.* **54** 1 (1983)]
8. Hancox C I et al. *Nature* **431** 281 (2004)
9. Chu X, Dalgarno A, Groenenboom G C *Phys. Rev. A* **75** 032723 (2007)
10. Buchachenko A A et al. *Phys. Scripta* **80** 048109 (2009)
11. Kolachevsky N et al. *Appl. Phys. B* **89** 589 (2007)
12. Connolly C B et al. *Phys. Rev. A* **81** 010702(R) (2010)
13. Ovsyannikov V D, Private discussions
14. Katori H et al. *Phys. Rev. Lett.* **91** 173005 (2003)
15. Ludlow A D et al. *Science* **319** 1805 (2008)
16. Melentiev P N et al. *Pis'ma Zh. Eksp. Teor. Fiz.* **83** 16 (2006) [*JETP Lett.* **83** 14 (2006)]
17. Goncharov A N et al., in *ICCNO/LAT: Int. Conf. on Coherent and Nonlinear Optics, Int. Conf. on Lasers, Applications, and Technologies, Kazan, 23 – 26 August 2010*, IWB3 p. 74
18. Ryabtsev I I et al. *Phys. Rev. Lett.* **104** 073003 (2010)
19. Martiyanov K, Makhalov V, Turlapov A *Phys. Rev. Lett.* **105** 030404 (2010)
20. Domnin Y et al., in *Precise Time and Time Interval: 41st PTTI Meeting, Santa Ana Pueblo, New Mexico, November 16 - 19, 2009*
21. Riehle F *Frequency Standards: Basics and Applications* (Weinheim: Wiley-VCH, 2004) [Translated into Russian (Moscow: Fizmatlit, 2009)]
22. Weiner J et al. *Rev. Mod. Phys.* **71** 1 (1999)
23. Leggett A J *Rev. Mod. Phys.* **73** 307 (2001)
24. Hachisu H et al. *Phys. Rev. Lett.* **100** 053001 (2008)
25. Brickman K-A et al. *Phys. Rev. A* **76** 043411 (2007)
26. Andresen G B et al. *Nature* **468** 673 (2010)
27. Cano D et al. *Phys. Rev. Lett.* **101** 183006 (2008)
28. Stuhler J et al. *Phys. Rev. Lett.* **95** 150406 (2005)
29. Sawyer B C et al. *Phys. Rev. Lett.* **98** 253002 (2007)
30. McClelland J J, Hanssen J L *Phys. Rev. Lett.* **96** 143005 (2006)
31. Lu M, Youn S H, Lev B L *Phys. Rev. Lett.* **104** 063001 (2010)
32. Chebakov K et al. *Opt. Lett.* **34** 2955 (2009)
33. Sukachev D et al. *Phys. Rev. A* **82** 011405(R) (2010)
34. Minogin V G, Letokhov V S *Davlenie Lazernogo Izlucheniya na Atomy* (Laser Light Pressure on Atoms) (Moscow: Nauka, 1986) [Translated into English (New York: Gordon and Breach Science Publ., 1987)]
35. Letokhov V S, Minogin V G, Pavlik B D *Zh. Eksp. Teor. Fiz.* **72** 1328 (1977) [*Sov. Phys. JETP* **45** 698 (1977)]
36. Dalibard J, Cohen-Tannoudji C *J. Opt. Soc. Am. B* **6** 2023 (1989)
37. Chang S et al. *Phys. Rev. A* **64** 013404 (2001)
38. Valentin C et al. *Europhys. Lett.* **17** 133 (1992)
39. Shang S-Q et al. *Phys. Rev. Lett.* **67** 1094 (1991)
40. Walhout M et al. *J. Opt. Soc. Am. B* **9** 1997 (1992)
41. Walhout M, Sterr U, Rolston S L *Phys. Rev. A* **54** 2275 (1996)
42. Berglund A J, Lee S A, McClelland J J *Phys. Rev. A* **76** 053418 (2007)
43. Stuhler J et al. *Phys. Rev. A* **64** 031405(R) (2001)